AIMS Mathematics, 10(12): 30732−30772.
DOI: 10.3934/math.20251349
Received: 29 September 2025
Revised: 06 December 2025
Accepted: 22 December 2025
Published: 29 December 2025

https://www.aimspress.com/journal/Math

Research article

Active control impact analysis on shaped coupled beam structure

Hany Samih Bauomy*

Department of Mathematics, College of Science and Humanities in Alkharj, Prince Sattam Bin Abdulaziz University, Alkharj 11942, Saudi Arabia

* **Correspondence:** Email: hany_samih@yahoo.com.

Abstract: Vibration-based warning and sensing devices rely on compact nonlinear structures capable of operating reliably under combined parametric and harmonic disturbances. To address these engineering demands, we developed a two-degree-of-freedom (2-DOF) lumped-parameter model that captures the coupled dynamics of a mass-based multi-warning unit integrated into a host structure. An II-shaped coupled beam was proposed as a practical realization of the concept, where an auxiliary "warning mass" interacts dynamically with a primary supporting beam through nonlinear oscillations. The governing nonlinear differential equations were analytically solved using the multiple-time-scale technique (MTST), with detailed emphasis on primary and internal resonance conditions ($\omega_d \cong \omega_1$, $\omega_e \cong \omega_2$) that critically influence device functionality and stability. To mitigate large-amplitude oscillations and enhance robustness under strong nonlinearities, a new control law, Nonlinear Proportional-Derivative Control with Negative Cubic Velocity Feedback (NPDCVF), was introduced. This controller combines a nonlinear PD term with a cubic dissipative component to improve damping and suppress resonance amplification. Control performance was assessed using the worst-case resonance scenario of the primary mass. Comparative simulations against Integral Resonance Control (IRC), Positive Position Feedback (PPF), Proportional-Integral-Derivative (PID), and Nonlinear Integral PPF (NIPPF) showed that the NPDCVF controller achieves up to 35–60% reduction in vibration amplitude, ensures faster settling, and maintains stable operation even near low natural frequencies where conventional controllers deteriorate. Frequency-response-based stability analysis revealed the boundaries of safe operation and highlighted instability regions relevant for design considerations. Numerical simulations using MATLAB/Simulink confirmed that the NPDCVF controller significantly enhances vibration suppression and flexibility against nonlinear disturbances. These results demonstrated the potential of the proposed system and control strategy for engineering applications such as structural warning devices, precision actuators, robotic manipulators, and advanced motorcycle suspension systems.

Keywords: lumped coupled parameter; investigated control; 1: 1 internal resonance; perturbation; shaped beam
Mathematics Subject Classification: 70K20, 74H45

Nomenclature

ω_1, ω_2	The normalized eigenstate mode frequency of the low frequency mode and the high frequency mode
ω_d, ω_e	The normalized frequencies of harmonic excitation applied on the low frequency mode and the high frequency mode
m_1, m_2	The effective mass of the low frequency mode and the high frequency mode
k_1, k_2	The linear stiffness of the low frequency mode and the high frequency mode
c_1, c_2	The modal damping of the low frequency mode and the high frequency mode
F	The amplitude of the harmonic excitation applied on the low frequency mode
Ω	The frequency of harmonic excitation applied on the low frequency mode
λ_1	The cubic nonlinear coupling term of the high frequency mode to the low frequency mode
χ_1	The nonlinear stiffness of the high frequency mode
χ_2	The cubic nonlinear coupling term of the low frequency mode to the high frequency mode
x_1, x_2	The displacements of the low frequency mode and the high frequency mode
μ_1, μ_2	The damping coefficients of the low frequency mode and the high frequency mode
α_1	The nonlinear spring constant of the high frequency mode
β_1, β_2	The nonlinear coupling coefficients of the low frequency mode to the high frequency mode and the high frequency mode to the low frequency mode
f, f_1, f_2	The normalized amplitudes of the harmonic excitation applied on the low frequency mode
ε	A small perturbation parameter

1. Introduction

Microelectromechanical systems (MEMS) have advanced rapidly over the past decade, enabling high-performance miniaturized structures for sensing, actuation, filtering, and timing applications. As device dimensions shrink, MEMS structures commonly exhibit strong nonlinear resonance behavior, including jump phenomena, hardening/softening stiffness characteristics, multi-frequency responses, and amplitude-dependent shifts in resonant frequency. These nonlinearities arise from geometric effects, electrostatic forces, material stiffness transitions, and multi-degree-of-freedom coupling, making the dynamic behavior of MEMS devices remarkably rich and complex. Internal resonance, in particular, occurs when two or more modes satisfy or approach a rational frequency ratio (e.g., 1:1 [1], 1:2 [2], 1:3 [3]), leading to intricate nonlinear modal interactions. Historically, internal resonance has been examined in rotating machinery [4], flexible structures [5,6], and naval platforms [7], but advancements in MEMS design and computation have renewed interest due to emerging applications in frequency conversion [8], micro-scale filtering [9], and energy harvesting [10]. The bifurcation of

internal resonance in a linear duffing system with cubic linked terms was theoretically investigated by Xu and Li [11]. Additionally, research has been done on nonlinear modal coupling in micromechanical resonators. One fundamental feature of internal resonance is the amplitude saturation phenomena [12–14]. Vibration suppression has made extensive use of this saturation property [15]. Younis [16] investigated the internal resonance of electrostatically driven MEMS arching beam resonators. Electric heating is used to modify the beam structure's modal frequency, causing arching beam scans to occur at 1:2 and 1:3 internal resonance. Additionally, the energy transfer between modes is discussed, and the frequency response of arching beam resonators at 1:2, 1:3, and 1:4 resonances is examined [17]. Dario Antonio et al. investigated the micro-beam resonator's 1:3 internal resonance, and the nonlinear energy transfer between the first-order and third-order modes achieves frequency stability [18]. There are several frequency components in the internal resonance system's response. Based on this, multi-frequency atomic mechanics microscopy was investigated by [19,20], which can increase higher harmonics and offer additional information for sample surface topography detection.

To contextualize the relevance of this work, it is important to highlight developments in MEMS resonator technologies, particularly the rise of graphene-based MEMS resonators in 2025. Traditional silicon resonators, while widely used, are limited by their relatively large mass, moderate stiffness, and modest electromechanical coupling. Graphene, by contrast, offers extraordinary material properties ultra-low mass density, exceptionally high Young's modulus (on the order of 1 TPa), and superior electrical conductivity which enable MEMS resonators with higher sensitivity, wider bandwidth, and more efficient transduction. Critically, these advantages come with significantly stronger nonlinear behavior. Experimental demonstrations from 2025 show that graphene MEMS resonators possess cubic nonlinear stiffness coefficients up to an order of magnitude larger than silicon resonators of similar geometry, resulting in enhanced amplitude–frequency coupling, pronounced jump phenomena, and stronger internal resonance effects. These amplified nonlinearities make graphene resonators more capable yet also more susceptible to instability, bifurcation, and energy transfer between coupled modes. Therefore, next-generation MEMS especially graphene-based devices require control frameworks capable of managing strong nonlinear effects while maintaining sensitivity, robustness, and stability. The II-shaped coupled-beam configuration proposed in this paper captures the essential dynamics relevant to such MEMS devices, including internal resonance, stiffness nonlinearity, and multi-mode coupling. The nonlinear multi-warning system built upon this configuration offers a representative platform to explore vibration mitigation strategies applicable to emerging MEMS technologies.

Controlling nonlinear dynamic systems, particularly in flexible and high-speed mechanical constructions, presents significant problems in the areas of strong stability maintenance and effective vibration suppression. The intricate nonlinearities and internal resonances that arise in these applications are frequently too complex for conventional linear controllers, such as PD and PID controllers. This has spurred the creation of sophisticated nonlinear control methods that provide better damping properties and flexibility. Robust stability and efficient vibration suppression are major problems in engineering systems, especially those that involve high-speed, flexible, and nonlinear dynamics, such robotic arms, aeronautical structures, and smart materials. These systems frequently display intricate behaviors that impair the effectiveness of traditional linear control techniques like PID or PD controllers, such as internal resonances, time delays, and nonlinear damping characteristics [21]. To overcome these restrictions, researchers have created a variety of nonlinear and adaptive control approaches. Among the most notable are Integral Resonance Control (IRC) [22], Positive Position Feedback (PPF) [23], and Nonlinear Integral Positive Position Feedback (NIPPF) controllers [24]. These approaches have showed potential in reducing resonant vibrations and enhancing damping without sacrificing control effort. However, their performance may be insufficient in systems with severe

nonlinearities, fast responses, or time-varying characteristics.

Nonlinear vibration has become a central topic in structural dynamics due to the increasing use of lightweight, flexible, and multi-functional engineering structures where linear assumptions fail to capture real behavior. Turning to materials and structural nonlinearities, Jiang et al. [25] investigated the effects of fiber orientation, graphene content, and temperature on the nonlinear flutter behavior of a graphene/carbon-fiber reinforced composite plate. Their experimental and theoretical study shows how geometric and material nonlinearity can interact to produce complex vibrational behaviors under aerodynamic loading. Similarly, Lian, et al. [26] wrote an Energy journal article and studied a bistable asymmetric cross-ply composite laminated (ACPCL) cantilever shell (relevant for morphing or adaptive structures such as wind turbine blades). They examined snap-through phenomena, resonances, bifurcations, and chaotic dynamics under combined external and parametric excitation, employing multiple-scale perturbation, and Melnikov methods. Their work highlights how nonlinear shell structures can exhibit rich, multi-pulse chaotic responses and fractal basin boundaries.

Vibration-based warning devices and compact sensing units are increasingly required in modern engineering systems such as robotic actuators, precision mechanisms, and motorcycle suspension assemblies. These systems often operate under strong nonlinearities, multi-source excitations, and resonance conditions that can cause performance degradation or unsafe dynamic amplification. The motivation of this study arises from the persistent challenge of controlling vibrations in nonlinear multi-degree-of-freedom systems under high-speed dynamics and resonance conditions. Conventional vibration control techniques (e.g., PID, IRC, PPF, and NIPPF) often struggle under these conditions because they assume near-linear behavior and lose stability at low natural frequencies or near strong resonances. Therefore, there is a growing need for lightweight, energy-efficient, and dynamically robust warning mechanisms that can sustain large variations in excitation while preserving stability and reliability. To address these challenges, we introduce a new mass-based multi-warning scheme implemented through an II-shaped coupled beam structure. This configuration enables a passive–active hybrid approach where the auxiliary warning mass interacts nonlinearly with the host structure to generate detectable dynamic responses. The manuscript also presents the Nonlinear Proportional-Derivative Controller with Negative Cubic Velocity Feedback (NPDCVF) as a novel control strategy specifically designed for nonlinear, resonance-prone, and low-frequency systems. Unlike classical controllers, the proposed NPDCVF introduces a nonlinear dissipative term that enhances damping during high-amplitude oscillations while maintaining sensitivity during low-amplitude states.

The novelty of this study lies in:

1) Developing a new 2-DOF nonlinear model for an auxiliary warning mass devices under both parametric and harmonic excitations.
2) Proposing an II-shaped coupled beam as a practical structural realization of such devices.
3) Introducing the NPDCVF controller, which integrates nonlinear PD action with a negative cubic velocity term to handle strong nonlinear resonance more effectively than existing controllers.
4) Providing a comprehensive comparison against IRC, PPF, PID, and NIPPF methods to demonstrate clear advantages in vibration reduction, stability maintenance, and low-frequency performance.
5) Establishing analytical MTST-based resonance characterization and frequency-response stability boundaries to guide practical design.

Together, these contributions provide a new pathway for designing high-sensitivity warning structures and robust nonlinear controllers suitable for next-generation vibration-sensitive devices.

Vibration-based warning and sensing devices are widely utilized in modern engineering systems, particularly in structural safety monitoring, transportation platforms, robotic mechanisms, and precision actuation units. These devices typically employ compact mechanical components, such as

miniaturized beams, auxiliary masses, or compliant mechanisms to detect abnormal dynamic conditions and initiate protective actions. In practical applications, these components often operate under simultaneous harmonic disturbances, parametric variations, environmental noise, and geometric nonlinearities arising from large deformations or material characteristics. Such factors introduce complex dynamic behavior that can significantly influence reliability, detection accuracy, and service life. A major challenge arises when the device operates near resonance or when internal resonances are activated due to multi-degree-of-freedom coupling. Under these conditions, even small disturbances may lead to large-amplitude oscillations, loss of sensitivity, or undesired triggering of warning signals. Traditional linear control methods (e.g., PID and PPF) and semi-linear approaches (e.g., IRC and NIPPF) typically perform well only within a limited frequency range and may lose effectiveness when cubic stiffness nonlinearities or strong amplitude-dependent dynamics dominate the system response. These limitations highlight the need for mechanically compact and dynamically robust systems capable of maintaining sensitivity and stability across different operating regimes.

Motivated by these practical engineering requirements, we propose an II-shaped coupled beam architecture as a compact 2-DOF warning–sensing unit. The configuration enables an auxiliary mass to interact dynamically with a primary structural beam, enabling enhanced energy transfer and improved detection capabilities under nonlinear oscillatory motion. Furthermore, to address the shortcomings of existing control schemes, a nonlinear control law, Nonlinear Proportional-Derivative Control with Negative Cubic Velocity Feedback (NPDCVF) is developed to provide improved damping, suppress resonance amplification, and maintain stable operation under strong nonlinear excitations. This engineering background establishes the practical motivation and contextual relevance of the proposed system and control strategy.

In this work, we present a unique control technique known as the Nonlinear Proportional-Derivative Controller with Negative Cubic Velocity Feedback (NPDCVF). This controller combines a nonlinear PD control law with a negative cubic velocity feedback term, which functions as a velocity-dependent nonlinear damper. The nonlinear PD component enables adaptive stiffness and damping behavior, and the cubic term improves system stability during high-amplitude or high-velocity oscillations while not influencing steady-state response [27]. The combination improves performance by suppressing transient oscillations, minimizing overshoot, and increasing robustness to external shocks and model uncertainty. To assess its effectiveness, the NPDCVF controller is compared to IRC, PPF, PID, and NIPPF controllers using numerical simulations on a two-degree-of-freedom lumped parameter system. The results show that the NPDCVF technique has substantial advantages, notably in terms of reducing large vibration amplitudes and preserving stability across a wide frequency range. These enhancements position the NPDCVF control technique as a promising contender for enhanced vibration control in applications such as flexible robots, structural health monitoring, and precision mechatronic systems [28,29]. Moreover, these results demonstrate the NPDCVF approach's promise for applications such as enhanced vibration control and robotic system actuation, where nonlinear dynamics are important. The rest of the paper is structured as follows: The control design and mathematical model are presented in Section 2. Comparative simulation results are presented in Section 3. The consequences for real-world deployment are covered in Section 4. The study is concluded in Section 5 with a summary and recommendations for additional research. In the proposed II-shaped coupled beam design, a fixed electrode placed beneath the free end of the primary beam enables electrostatic tuning of the effective nonlinear stiffness, an approach widely adopted in MEMS resonators. However, such tenability inherently introduces the Pull-in phenomenon, in which the electrostatic attraction exceeds the structural restoring force and causes a sudden collapse of the beam onto the electrode. This instability not only threatens structural integrity but also disrupts the intended

stiffness-modulation mechanism, thereby affecting both the reliability of the multi-warning scheme and the overall performance of the NPDCVF controller. Recent findings [30] provide several practical mitigation strategies that can be adapted to the present architecture. These include geometric stiffening of critical beam sections, integrating dielectric or mechanical stoppers to limit excessive deflection, optimizing electrode spacing and shape to reduce electrostatic field gradients, and regulating the bias voltage through closed-loop control. Incorporating these measures broadens the safe operational window of the electrostatically tuned structure and strengthens its viability for MEMS-scale vibration-warning and control applications.

2. Deducing equations of dynamical modeling

The development of the proposed mass-based multi-warning scheme is rooted in the practical need for early detection and suppression of resonance in lightweight and weakly damped structures that operate under multi-source excitations. In many engineering applications, such as slender mechanical frames, flexible robotic arms, motorcycle suspensions, and compact structural components, the primary structure often exhibits low natural frequencies and amplitude-dependent stiffness, making it highly sensitive to harmonic or parametric excitation. Traditional single-mass warning mechanisms or threshold sensors are unable to capture the subtle onset of resonance because they do not amplify structural motion nor reflect coupled dynamic effects. To overcome this limitation, we model the system as a two-degree-of-freedom (2-DOF) lumped parameter structure, where a secondary "warning mass" is mechanically attached to the main structure through elastic and damping elements. The proposed two-degree-of-freedom (2-DOF) lumped-parameter model is developed to capture the essential dynamics of a mass-based multi-warning system, where an auxiliary warning mass interacts dynamically with a primary structure. Such systems are widely employed in vibration mitigation, energy harvesting, and mechanical warning devices, where a secondary mass is deliberately coupled to a primary structure to absorb energy at critical resonance frequencies. The primary mass represents the main structure subject to external excitations, while the auxiliary mass is designed to respond preferentially to the most critical resonance modes. The coupling springs and dampers model the mechanical connections or structural attachments that enable energy transfer and vibration suppression between the two masses. The physical realization of this system can be achieved through an II-shaped coupled beam structure, consisting of a rectangular beam connected via two overhangs to the II-shaped main beam. This configuration enables controlled stiffness and damping characteristics, which are essential for achieving the desired dynamic interaction between the primary and auxiliary masses. By capturing the key physical phenomena, including energy redistribution, resonance amplification, and damping effects, the lumped-parameter model serves as a realistic representation of practical engineering systems such as robotic actuators, vehicle suspensions, and auxiliary vibration suppression devices.

To estimate the system response, the two-degree-of-freedom lumped parameter model of the proposed mass multi warning scheme is given in Figure 1. Motions of the nonlinear mode low frequency mode (LFM) and the linear mode high frequency mode (HFM) are coupled by the nonlinear terms of $\chi_2 x_1^3$ and $\chi_1 x_1 x_2^2$. All the parameters are defined in the nomenclature. Applying Newton's second law to each mass, the dynamic behavior of the system is described by the following coupled second-order differential equations:

$$m_1\ddot{x}_1 + c_1\dot{x}_1 + k_1x_1 + \lambda_1x_1^3 + \chi_1 x_1 x_2^2 = F\cos(\Omega t^*) \tag{1}$$

$$m_2\ddot{x}_2 + c_2\dot{x}_2 + k_2x_2 + \chi_2 x_1^3 = 0. \tag{2}$$

Here, F, Ω are the amplitude and angular frequency of the harmonic excitation applied on LFM. A small perturbation parameter, ε, is introduced into Eqs (1) and (2) to indicate that the modal damping, the nonlinear stiffness, and the cubic nonlinear coupling term and harmonic excitation force are small. Therefore, Eqs (3) and (4) can be obtain by normalizing Eqs (1) and (2) with the dimensionless time $t = t^* \sqrt{k_1 / m_1}$.

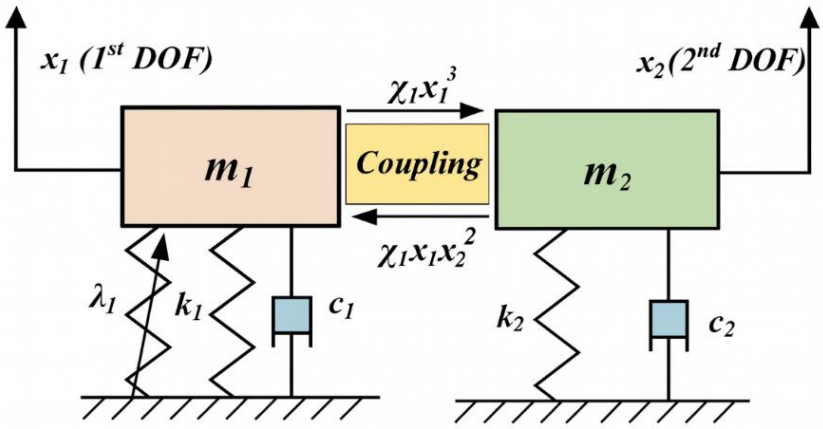

Figure 1. Two-degree-of-freedom lumped parameter model of the proposed mass multi-warning scheme.

Equations (1) and (2) are derived by applying Newton's second law to each mass, accounting for elastic restoring forces, damping forces, and nonlinear feedback control inputs. The resulting coupled second-order differential equations not only describe the inherent dynamics of the system but also provide a mathematical foundation for designing and validating the NPDCVF controller. By grounding the model in realistic physical behavior, it is ensured that the subsequent control analysis and simulation results are directly applicable to real-world engineering systems such as robotic actuators, vehicle suspensions, and auxiliary vibration suppression devices.

$$\ddot{x}_1 + \omega_1^2 x_1 = \varepsilon\left[-\mu_1 \dot{x}_1 - \alpha_1 x_1^3 - \beta_1 x_1 x_2^2 + f\cos(\omega_d t)\right] \tag{3}$$

$$\ddot{x}_2 + \omega_2^2 x_2 = \varepsilon\left[-\mu_2 \dot{x}_2 - \beta_2 x_1^3\right]. \tag{4}$$

Here, $\omega_1 = 1, \mu_1 = \dfrac{c_1}{\varepsilon\sqrt{m_1 k_1}}, \alpha_1 = \dfrac{\lambda_1}{\varepsilon k_1}, \beta_1 = \dfrac{\chi_1}{\varepsilon k_1}, f = \dfrac{F}{\varepsilon k_1}, \omega_d = \Omega\sqrt{\dfrac{m_1}{k_1}}$

and $\omega_2 = \sqrt{\dfrac{m_1 k_2}{m_2 k_1}} = 3$, $\mu_2 = \dfrac{c_2}{\varepsilon m_2}\sqrt{\dfrac{m_1}{k_1}}, \beta_2 = \dfrac{\chi_2}{\varepsilon m_2}\dfrac{m_1}{k_1}, \omega_e = \Omega\sqrt{\dfrac{m_2}{k_2}}$.

A two-degree-of-freedom lumped parameter model and the corresponding governing equations have been given for theoretical study. How to physically realize the mass multi-warning scheme is one of the most important contents of this paper. As we can see from Eqs (3) and (4), the nonlinear coupling terms are $x_1 x_2^2$ and x_1^3 for the two modes respectively, both of which are cubic terms. The most common cubic nonlinear term in MEMS resonators is duffing nonlinearity. Therefore, the duffing nonlinear term $(x_1 - x_2)^3$ is used as the coupling term for physically realizing the multi-warning

scheme. An II-shaped coupled beam structure, consisting of an II -shaped beam and a rectangular beam that coupled by two overhangs, is further proposed, as shown in Figure 2. The frequency ratio of the flexural mode of the II -shaped beam and the rectangular beam is designed to be about 1:3. Two piezo films are attached on the fixed end of the G-shaped beam for detecting. Mass perturbation is applied on the tip of the rectangular beam. A fixed electrode plate is placed under the free end of the II -shaped beam to form a capacitor, so as to adjust the nonlinear stiffness of the II -shaped beam. Through theoretical derivation, it is found that the effective components of the duffing nonlinear coupling term $(x_1 - x_2)^3$ for the II -shaped beam are $x_1^2 x_2$ and $x_1 x_2^2$, while that for the rectangular beam are $x_1^2 x_2$ and x_1^3, which are similar to those in Eqs (3) and (4), but more complicated. When the II -shaped coupled beam structure is excited into resonance by a harmonic excitation, the normalized coupled motion of the two beams under harmonic excitation are given by the following equations,

$$\ddot{x}_1 + \omega_1^2 x_1 = \varepsilon\left[-\mu_1 \dot{x}_1 - \alpha_1 x_1^3 - \beta_1 (x_1 - x_2)^3 + f_1 \cos(\omega_d t) + f_1 x_1 \cos(\omega_d t)\right] \tag{5}$$

$$\ddot{x}_2 + \omega_2^2 x_2 = \varepsilon\left[-\mu_2 \dot{x}_2 - \alpha_2 x_2^3 - \beta_2 (x_2 - x_1)^3 + f_2 \cos(\omega_e t) + f_2 x_2 \cos(\omega_e t)\right]. \tag{6}$$

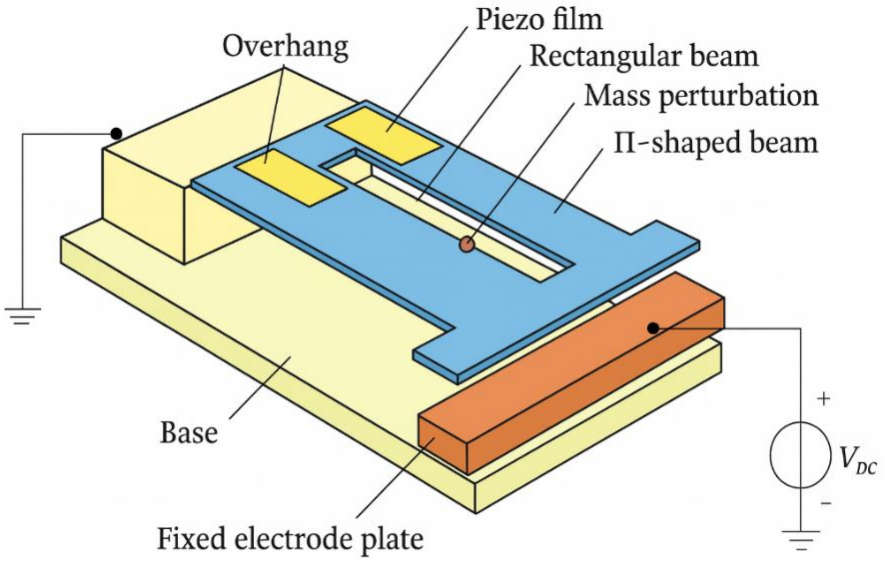

Figure 2. Physical mode for the proposed mass multi-warning scheme, consisting of an II -shaped beam and a rectangular beam that coupled by two overhangs. The frequency ratio of the flexural mode of the II -shaped beam and the rectangular beam is designed to be 1:1. Mass perturbation is applied on the tip of the rectangular beam. A fixed electrode plate is placed under the free end of the II -shaped beam to form a capacitor to adjust the nonlinear stiffness of the II -shaped beam.

3. Equations of the modeling system with perturbation analysis

After adding the novel NPDCVF controller, the redesigned model system Eqs (5,6) ([31]) are examined as follows:

$$\ddot{x}_1 + \omega_1^2 x_1 = \varepsilon\left[-\mu_1 \dot{x}_1 - \alpha_1 x_1^3 - \beta_1 (x_1 - x_2)^3 + f_1 \cos(\omega_d t) + f_1 x_1 \cos(\omega_d t)\right] + F_{1c}(t) \tag{7a}$$

$$\ddot{x}_2+\omega_2^2x_2=\varepsilon\left[-\mu_2\dot{x}_2-\alpha_2x_2^3-\beta_2(x_2-x_1)^3+f_2\cos(\omega_e t)+f_2\ x_2\cos(\omega_e t)\right]+F_{2c}(t). \tag{7b}$$

Here, $F_{1c}(t)$ and $F_{2c}(t)$ remain the control inputs to reduce the vibration that occurs at the primary resonance item ($\omega_d\cong\omega_1$, $\omega_e\cong\omega_2$) with NPDCVF controller given by:

$$F_{1c}(t)=-\varepsilon(p_1x_1+\mathrm{d}_1\dot{x}_1+\alpha_3x_1^3+\alpha_4x_1^2\dot{x}_1+\alpha_5x_1\dot{x}_1^2+\mathrm{G}_1\dot{x}_1^3), \tag{8a}$$

$$F_{2c}(t)=-\varepsilon(p_2x_2+\mathrm{d}_2\dot{x}_2+\alpha_6x_2^3+\alpha_7x_2^2\dot{x}_2+\alpha_8x_2\dot{x}_2^2+\mathrm{G}_2\dot{x}_2^3). \tag{8b}$$

3.1. Mathematical examination through the perturbation technique

Using a novel control procedure NPDCVF controller, the controlled model equations are provided as:

$$\begin{aligned}\ddot{x}_1+\omega_1^2x_1=&\varepsilon\left[-\mu_1\dot{x}_1-\alpha_1x_1^3-\beta_1(x_1-x_2)^3+f_1\cos(\omega_d t)+f_1x_1\cos(\omega_d t)\right]\\&-\varepsilon(p_1x_1+\mathrm{d}_1\dot{x}_1+\alpha_3x_1^3+\alpha_4x_1^2\dot{x}_1+\alpha_5x_1\dot{x}_1^2+\mathrm{G}_1\dot{x}_1^3),\end{aligned} \tag{9a}$$

$$\begin{aligned}\ddot{x}_2+\omega_2^2x_2=&\varepsilon\left[-\mu_2\dot{x}_2-\alpha_2x_2^3-\beta_2(x_2-x_1)^3+f_2\cos(\omega_e t)+f_2\ x_2\cos(\omega_e t)\right]\\&-\varepsilon(p_2x_2+\mathrm{d}_2\dot{x}_2+\alpha_6x_2^3+\alpha_7x_2^2\dot{x}_2+\alpha_8x_2\dot{x}_2^2+\mathrm{G}_2\dot{x}_2^3).\end{aligned} \tag{9b}$$

Here, $(p_1x_1+\mathrm{d}_1\dot{x}_1),(p_2x_2+\mathrm{d}_2\dot{x}_2)$ are the linear control forces, and $(\alpha_3x_1^3+\alpha_4x_1^2\dot{x}_1+\alpha_5x_1\dot{x}_1^2)$, $(\alpha_6x_2^3+\alpha_7x_2^2\dot{x}_2+\alpha_8x_2\dot{x}_2^2)$ stand the non-linear control forces, and G_1,G_2 are the gains as illustrated in Figure 3.

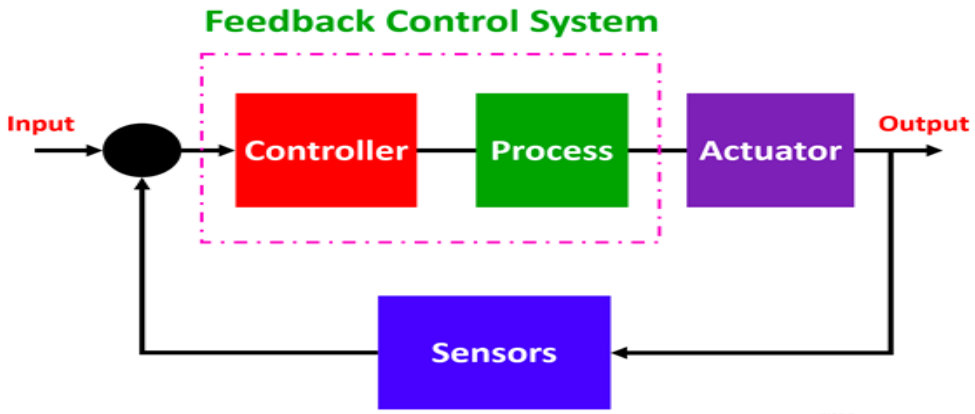

Figure 3. A feedback control system is a system that regulates itself by continuously comparing its output to a desired output (reference) and using the difference, called an error, to adjust its input. This closed-loop approach ensures the system maintains the desired output by correcting for deviations.

We seek a first-order uniform expansion by the MTSM [32−34] in the form as Eq (9).

$$x_1(t;\varepsilon)=x_{10}(T_0,T_1)+\varepsilon x_{11}(T_0,T_1)+O(\varepsilon^2) \tag{10a}$$

$$x_2(t;\varepsilon) = x_{20}(T_0, T_1) + \varepsilon x_{21}(T_0, T_1) + O(\varepsilon^2) . \tag{10b}$$

The time-related derivatives are provided by:

$$\frac{d}{dt} = D_0 + \varepsilon D_1, \frac{d^2}{dt^2} = D_0^2 + 2\varepsilon D_0 D_1 \quad . \tag{11}$$

Here, $T_n = \varepsilon^n t (n = 0,1)$. T_0 and T_1 are the fast and slow time scales, respectively.

Using Eq (11), we can substitute Eq (10) in Eq (9) and compare the coefficients of equivalent power of ε on both sides to acquire:

$$O(\varepsilon): (D_0^2 + \omega_1^2) x_{10} = 0 \tag{12a}$$

$$(D_0^2 + \omega_2^2) x_{20} = 0 \tag{12b}$$

$$O(\varepsilon^1): (D_0^2 + \omega_1^2) x_{11} = -2D_0 D_1 x_{10} - \mu_1 D_0 x_{10} - \alpha_1 x_{10}^3 - \beta_1 (x_{10} - x_{20})^3 + f_1 \cos(\omega_d t)$$

$$+ f_1 x_{10} \cos(\omega_d t) - p_1 x_{10} - d_1 D_0 x_{10} - \alpha_3 x_{10}^3 - \alpha_4 x_{10}^2 D_0 x_{10} - \alpha_5 x_{10} \left(D_0 x_{10}\right)^2 - G_1 (D_0 x_{10})^3 \tag{13a}$$

$$(D_0^2 + \omega_2^2) x_{21} = -2D_0 D_1 x_{20} - \mu_2 D_0 x_{20} - \alpha_2 x_{20}^3 - \beta_2 (x_{20} - x_{10})^3 + f_2 \cos(\omega_e t)$$

$$+ f_2 x_{20} \cos(\omega_e t) - p_2 x_{20} - d_2 D_0 x_{20} - \alpha_6 x_{20}^3 - \alpha_7 x_{20}^2 D_0 x_{20} - \alpha_8 x_{20} \left(D_0 x_{20}\right)^2 - G_2 (D_0 x_{20})^3 \ . \tag{13b}$$

The following formula provides the solution to Eq (12):

$$x_{10} = A_1 e^{i\omega_1 T_0} + cc \tag{14a}$$

$$x_{20} = A_2 e^{i\omega_2 T_0} + cc . \tag{14b}$$

Here, A_1 and A_2 indicate a complex function that has been verified by removing small-divisor and secular terms from the first approximations. It also shows the complex conjugates of the terms that came before it. When Eq (14) is substituted into Eq (13), and the secular terms are eliminated, the specific solutions of Eq (13) are:

$$x_{11} = \begin{bmatrix} -2i\omega_1 D_1 A_1 - i\omega_1 \mu_1 A_1 - 3\alpha_1 A_1^2 \bar{A}_1 - 3\beta_1 A_1^2 \bar{A}_1 - 6\beta_1 A_1 A_2 \bar{A}_2 - p_1 A_1 - i\omega_1 d_1 A_1 \\ -3\alpha_3 A_1^2 \bar{A}_1 - i\omega_1 \alpha_4 A_1^2 \bar{A}_1 - \omega_1^2 \alpha_5 A_1^2 \bar{A}_1 - 3i\omega_1^3 G_1 A_1^2 \bar{A}_1 \end{bmatrix} e^{i\omega_1 T_0}$$

$$+ \left[-\alpha_1 A_1^3 - \beta_1 A_1^3 - \alpha_3 A_1^3 - i\omega_1 \alpha_4 A_1^3 + \omega_1^2 \alpha_5 A_1^3 + i\omega_1^3 G_1 A_1^3 \right] e^{3i\omega_1 T_0}$$

$$+ \left[3\beta_1 A_2^2 \bar{A}_2 + 6\beta_1 A_1 \bar{A}_1 A_2 \right] e^{i\omega_2 T_0} + \left[\beta_1 A_2^3 \right] e^{3i\omega_2 T_0} + \left[-3\beta_1 A_1 A_2^2 \right] e^{i(\omega_1 + 2\omega_2) T_0}$$

$$+ \left[-3\beta_1 A_1 \bar{A}_2^2 \right] e^{i(\omega_1 - 2\omega_2) T_0} + \left[3\beta_1 A_1^2 A_2 \right] e^{i(2\omega_1 + \omega_2) T_0} + \left[3\beta_1 A_1^2 \bar{A}_2 \right] e^{i(2\omega_1 - \omega_2) T_0}$$

$$+ \left[\frac{1}{2} f_1 \right] e^{i\omega_d T_0} + \left[\frac{1}{2} f_1 A_1 \right] e^{i(\omega_d + \omega_1) T_0} + \left[\frac{1}{2} f_1 \bar{A}_1 \right] e^{i(\omega_d - \omega_1) T_0} \tag{15a}$$

$$x_{21} = \begin{bmatrix} -2i\omega_2 D_1 A_2 - i\omega_2 \mu_2 A_2 - 3\alpha_2 A_2^2 \bar{A}_2 - 3\beta_2 A_2^2 \bar{A}_2 - 6\beta_2 A_2 A_1 \bar{A}_1 - p_2 A_2 - i\omega_2 d_2 A_2 \\ -3\alpha_6 A_2^2 \bar{A}_2 - i\omega_2 \alpha_7 A_2^2 \bar{A}_2 - \omega_2^2 \alpha_8 A_2^2 \bar{A}_2 - 3i\omega_2^3 G_2 A_2^2 \bar{A}_2 \end{bmatrix} e^{i\omega_2 T_0}$$

$$+ \left[-\alpha_2 A_2^3 - \beta_2 A_2^3 - \alpha_6 A_2^3 - i\omega_2 \alpha_7 A_2^3 + \omega_2^2 \alpha_8 A_2^3 + i\omega_2^3 G_2 A_2^3 \right] e^{3i\omega_2 T_0}$$

$$+\left[3\beta_2 A_1^2\bar{A}_1+6\beta_2 A_2\bar{A}_2 A_1\right]e^{i\omega_1 T_0}+\left[\beta_2 A_1^3\right]e^{3i\omega_1 T_0}+\left[-3\beta_2 A_2 A_1^2\right]e^{i(\omega_2+2\omega_1)T_0}$$
$$+\left[-3\beta_2 A_2\bar{A}_1^2\right]e^{i(\omega_2-2\omega_1)T_0}+\left[3\beta_2 A_2^2 A_1\right]e^{i(2\omega_2+\omega_1)T_0}+\left[3\beta_2 A_2^2\bar{A}_1\right]e^{i(2\omega_2-\omega_1)T_0}$$
$$+\left[\frac{1}{2}f_2\right]e^{i\omega_e T_0}+\left[\frac{1}{2}f_2 A_2\right]e^{i(\omega_e+\omega_2)T_0}+\left[\frac{1}{2}f_2\bar{A}_2\right]e^{i(\omega_e-\omega_2)T_0}. \tag{15b}$$

3.2. Classification of resonance and modulation equations

In this section, our goals are to categorize resonance cases, address one of them, and obtain the modulation equations. If any of the denominators in the final two solution approaches disappear, such circumstances might appear [35,36]. Consequently, the following opportunities arise. We separate and arrange each resonance scenario from the given solutions as follows:

• Primary resonance: $\omega_d \cong \omega_1, \omega_e \cong \omega_2$;

• Internal resonance: $\omega_1 \cong 2\omega_2, \omega_2 \cong 2\omega_1$;

• Simultaneous resonance: Any combined previous resonance cases.

If any of the mentioned criteria for resonance are fulfilled, the system under examination will exhibit highly complex behavior. It is crucial to remember that the solutions generated are suitable even while the oscillations are far from resonance. Moreover, it is crucial to remember that the solutions generated are suitable even when the oscillations are far from resonance. Now, let us take a closer look at the problem and examine the worst-case resonance, which is the primary resonance that occurs, $\omega_d \cong \omega_1, \omega_e \cong \omega_2$. Then, one can consider the detuning parameters σ_1 and σ_2 that contribute to achieving this objective, which indicates the closeness of ω_d and ω_e to ω_1 and ω_2, respectively. Therefore, one writes

$$\omega_d \cong \omega_1 + \varepsilon\sigma_1, \omega_e \cong \omega_2 + \varepsilon\sigma_2. \tag{16}$$

Equation (16) describes the steady-state dynamic response of the system under mixed harmonic and parametric excitations. In the current resonance case, the excitation frequencies ω_d, ω_e are assumed to be close to the natural frequency of the primary modes ω_1, ω_2. To analytically capture this near-resonant condition within the MTST framework, the excitation frequencies are expressed using the standard detuning relations:

$$\omega_d \cong \omega_1 + \varepsilon\sigma_1, \quad \omega_e \cong \omega_2 + \varepsilon\sigma_2,$$

where $\varepsilon \ll 1$ is a bookkeeping parameter, and σ_1, σ_2 are detuning coefficients that quantify how close the system is to exact harmonic and parametric resonance. These expressions enable small deviations from the natural frequencies to be systematically incorporated into the first-order modulation equations. Under this assumption, the denominator of the response term in (16) contains the near-singular factor $(\omega_1^2 - \omega_d^2), (\omega_2^2 - \omega_e^2)$, which becomes very small as $\omega_d \to \omega_1, \omega_e \to \omega_2$, resulting in significant amplification of the oscillatory response. Physically, this condition means that energy is transferred from the excitation source to the structure with maximum efficiency. As a result, the primary mass exhibits large-amplitude oscillations, and the relative displacement between the two masses is magnified. In this regime, nonlinear stiffness, internal resonance, and amplitude-dependent frequency shifts become increasingly influential. These nonlinearities distort the resonance peak, generate higher harmonics, and can even lead to multi-stable responses or jump phenomena. Because the proposed

mass-based multi-warning scheme is intended to detect and control excessive vibrations, the current resonance case represents the most critical operating scenario. Without adequate vibration suppression, the system may experience instability, high stresses, or undesired activation of the warning mass. Therefore, detailed analysis of this resonance condition justifies the use of the proposed NPDCVF controller, which provides additional nonlinear damping and stabilizing action precisely when the excitation frequency lies within the detuning range defined by

$$\omega_d \cong \omega_1 + \varepsilon\sigma_1, \quad \omega_e \cong \omega_2 + \varepsilon\sigma_2 .$$

This resonance scenario is critical to this study because it represents the worst operating condition, where uncontrolled oscillations may lead to structural fatigue, instability, or loss of functional performance. Accordingly, analyzing the current resonance case provides justification for implementing the proposed NPDCVF control strategy, which is designed to suppress excessive vibration levels and maintain stable operation even when the excitation frequency is very close to the natural frequency. This ensures safe and stable performance even in the presence of strong resonance amplification.

The solvability conditions for the first order approximations are obtained by substituting Eq (16) into Eq (13), and removing the secular terms. We observe that A_1 and A_2 are functions in T_1, and we obtain:

$$\begin{aligned} 2i\omega_1 D_1 A_1 = &-i\omega_1\mu_1 A_1 - 3\alpha_1 A_1^2\bar{A}_1 - 3\beta_1 A_1^2\bar{A}_1 - 6\beta_1 A_1 A_2\bar{A}_2 + \frac{f_1}{2}e^{i\sigma_1 T_1} \\ &- p_1 A_1 - i\omega_1 d_1 A_1 - 3\alpha_3 A_1^2\bar{A}_1 - i\omega_1\alpha_4 A_1^2\bar{A}_1 - \omega_1^2\alpha_5 A_1^2\bar{A}_1 - 3i\omega_1^3 G_1 A_1^2\bar{A}_1 \end{aligned} \tag{17a}$$

$$\begin{aligned} 2i\omega_2 D_1 A_2 = &-i\omega_2\mu_2 A_2 - 3\alpha_2 A_2^2\bar{A}_2 - 3\beta_2 A_2^2\bar{A}_2 - 6\beta_2 A_2 A_1\bar{A}_1 + \frac{f_2}{2}e^{i\sigma_2 T_1} \\ &- p_2 A_2 - i\omega_2 d_2 A_2 - 3\alpha_6 A_2^2\bar{A}_2 - i\omega_2\alpha_7 A_2^2\bar{A}_2 - \omega_2^2\alpha_8 A_2^2\bar{A}_2 - 3i\omega_2^3 G_2 A_2^2\bar{A}_2 \end{aligned} . \tag{17b}$$

To distinguish the averaging conditions that manage the components of Eq (17), let definite A_1, A_2 and $\bar{A}_1, \bar{A}_2$ be expressed in the resulting polar expressions

$$A_1 = \frac{1}{2}a_1(T_1)e^{i\gamma_1(T_1)}, \bar{A}_1 = \frac{1}{2}a_1(T_1)e^{-i\gamma_1(T_1)} \tag{18a}$$

$$A_2 = \frac{1}{2}a_2(T_1)e^{i\gamma_2(T_1)}, \quad \bar{A}_2 = \frac{1}{2}a_2(T_1)e^{-i\gamma_2(T_1)} . \tag{18b}$$

Here, a_1, a_2 and γ_1, γ_2 are the steady-state amplitudes and phases, respectively. Substituting Eq (18) in Eq (17), we get the modulation equations:

$$\begin{aligned} i\omega_1 a_1' - \omega_1 a_1\gamma_1' = &-\frac{1}{8}\left[3\alpha_1 + 3\beta_1 + 3\alpha_3 + i\omega_1\alpha_4 + \omega_1^2\alpha_5 + 3i\omega_1^3 G_1\right]a_1^3 \\ &-\frac{1}{2}\left[i\omega_1\mu_1 + p_1 + i\omega_1 d_1\right]a_1 - \frac{6}{8}\beta_1 a_1 a_2^2 + \frac{f_1}{2}e^{i(\sigma_1 T_1 - \gamma_1)} \end{aligned} \tag{19a}$$

$$\begin{aligned} i\omega_2 a_2' - \omega_2 a_2\gamma_2' = &-\frac{1}{8}\left[3\alpha_2 + 3\beta_2 + 3\alpha_6 + i\omega_2\alpha_7 + \omega_2^2\alpha_8 + 3i\omega_2^3 G_2\right]a_2^3 \\ &-\frac{1}{2}\left[i\omega_2\mu_2 + p_2 + i\omega_2 d_2\right]a_2 - \frac{6}{8}\beta_2 a_2 a_1^2 + \frac{f_2}{2}e^{i(\sigma_2 T_1 - \gamma_2)} \end{aligned} . \tag{19b}$$

Then, separating imaginary and real components of Eq (19), we get:

$$a_1' = -\frac{1}{8}\left[\alpha_4 + 3\omega_1^2 G_1\right]a_1^3 - \frac{1}{2}\left[\mu_1 + d_1\right]a_1 + \frac{f_1}{2\omega_1}\sin\theta_1 \tag{20a}$$

$$a_1\gamma_1' = \frac{1}{8}\left[\frac{3\alpha_1}{\omega_1} + \frac{3\beta_1}{\omega_1} + \frac{3\alpha_3}{\omega_1} + \omega_1\alpha_5\right]a_1^3 + \frac{1}{2}\left[\frac{p_1}{\omega_1}\right]a_1 + \frac{6}{8}\frac{\beta_1}{\omega_1}a_1a_2^2 - \frac{f_1}{2\omega_1}\cos\theta_1 \tag{20b}$$

$$a_2' = -\frac{1}{8}\left[\alpha_7 + 3\omega_2^2 G_2\right]a_2^3 - \frac{1}{2}\left[\mu_2 + d_2\right]a_2 + \frac{f_2}{2\omega_2}\sin\theta_2 \tag{21a}$$

$$a_2\gamma_2' = \frac{1}{8}\left[\frac{3\alpha_2}{\omega_2} + \frac{3\beta_2}{\omega_2} + \frac{3\alpha_6}{\omega_2} + \omega_2\alpha_7\right]a_2^3 + \frac{1}{2}\left[\frac{p_2}{\omega_2}\right]a_2 + \frac{6}{8}\frac{\beta_2}{\omega_2}a_2a_1^2 - \frac{f_2}{2\omega_2}\cos\theta_2 . \tag{21b}$$

Here,

$$\theta_1 = \sigma_1 T_1 - \gamma_1,\ \theta_2 = \sigma_2 T_1 - \gamma_2 . \tag{22}$$

Then,

$$\theta_1' = \sigma_1 - \gamma_1',\ \theta_2' = \sigma_2 - \gamma_2' . \tag{23}$$

Substitute Eq (23) into Eqs (20) and (21) to obtain the following:

$$a_1' = -\frac{1}{8}\left[\alpha_4 + 3\omega_1^2 G_1\right]a_1^3 - \frac{1}{2}\left[\mu_1 + d_1\right]a_1 + \frac{f_1}{2\omega_1}\sin\theta_1 \tag{24a}$$

$$a_1(\sigma_1 - \theta_1') = \frac{1}{8}\left[\frac{3\alpha_1}{\omega_1} + \frac{3\beta_1}{\omega_1} + \frac{3\alpha_3}{\omega_1} + \omega_1\alpha_5\right]a_1^3 + \frac{1}{2}\left[\frac{p_1}{\omega_1}\right]a_1 + \frac{6}{8}\frac{\beta_1}{\omega_1}a_1a_2^2 - \frac{f_1}{2\omega_1}\cos\theta_1 \tag{24b}$$

$$a_2' = -\frac{1}{8}\left[\alpha_7 + 3\omega_2^2 G_2\right]a_2^3 - \frac{1}{2}\left[\mu_2 + d_2\right]a_2 + \frac{f_2}{2\omega_2}\sin\theta_2 \tag{25a}$$

$$a_2(\sigma_2 - \theta_2') = \frac{1}{8}\left[\frac{3\alpha_2}{\omega_2} + \frac{3\beta_2}{\omega_2} + \frac{3\alpha_6}{\omega_2} + \omega_2\alpha_7\right]a_2^3 + \frac{1}{2}\left[\frac{p_2}{\omega_2}\right]a_2 + \frac{6}{8}\frac{\beta_2}{\omega_2}a_2a_1^2 - \frac{f_2}{2\omega_2}\cos\theta_2 . \tag{25b}$$

For steady-state responses ($a_1' = a_2' = \theta_1' = \theta_2' = 0$) and $\gamma_1' = \sigma_1$, $\gamma_2' = \sigma_2$, then Eqs (24) and (25) yield the steady state solutions, which are as follows:

$$-\frac{1}{8}\left[\alpha_4 + 3\omega_1^2 G_1\right]a_1^3 - \frac{1}{2}\left[\mu_1 + d_1\right]a_1 + \frac{f_1}{2\omega_1}\sin\theta_1 = 0 \tag{26a}$$

$$a_1\sigma_1 = \frac{1}{8}\left[\frac{3\alpha_1}{\omega_1} + \frac{3\beta_1}{\omega_1} + \frac{3\alpha_3}{\omega_1} + \omega_1\alpha_5\right]a_1^3 + \frac{1}{2}\left[\frac{p_1}{\omega_1}\right]a_1 + \frac{6}{8}\frac{\beta_1}{\omega_1}a_1a_2^2 - \frac{f_1}{2\omega_1}\cos\theta_1 \tag{26b}$$

$$-\frac{1}{8}\left[\alpha_7 + 3\omega_2^2 G_2\right]a_2^3 - \frac{1}{2}\left[\mu_2 + d_2\right]a_2 + \frac{f_2}{2\omega_2}\sin\theta_2 = 0 \tag{27a}$$

$$a_2\sigma_2 = \frac{1}{8}\left[\frac{3\alpha_2}{\omega_2}+\frac{3\beta_2}{\omega_2}+\frac{3\alpha_6}{\omega_2}+\omega_2\alpha_7\right]a_2^3+\frac{1}{2}\left[\frac{p_2}{\omega_2}\right]a_2+\frac{6}{8}\frac{\beta_2}{\omega_2}a_2a_1^2-\frac{f_2}{2\omega_2}\cos\theta_2 \quad . \tag{27b}$$

The following is a formal stability analysis of the steady-state structure using the Lyapunov first technique to get the eigenvalues of the right-hand side of the Jacobian matrix pointed at Eqs (24) and (25):

$$\begin{bmatrix} a_1' \\ \theta_1' \\ a_2' \\ \theta_2' \end{bmatrix} = \begin{bmatrix} R_{11} & R_{12} & R_{13} & R_{14} \\ R_{21} & R_{22} & R_{23} & R_{24} \\ R_{31} & R_{32} & R_{33} & R_{34} \\ R_{41} & R_{42} & R_{43} & R_{44} \end{bmatrix} \begin{bmatrix} a_1 \\ \theta_1 \\ a_2 \\ \theta_2 \end{bmatrix}. \tag{28}$$

Here, the factors $R_{jk}: j=1,2,3,4, k=1,2,3,4$ are defined in Appendix A. The previous matrix obtains the stable regions of the controlled model by resolving the subsequent determinant:

$$\begin{vmatrix} R_{11}-\lambda & R_{12} & R_{13} & R_{14} \\ R_{21} & R_{22}-\lambda & R_{23} & R_{24} \\ R_{31} & R_{32} & R_{33}-\lambda & R_{34} \\ R_{41} & R_{42} & R_{43} & R_{44}-\lambda \end{vmatrix} = 0 . \tag{29}$$

Then,

$$\lambda^4 + r_1\lambda^3 + r_2\lambda^2 + r_3\lambda + r_4 = 0 . \tag{30}$$

Here, λ indicates the Jacobian matrix's eigenvalue, and r_1, r_2, r_3, and r_4 are the coefficients of Eq (36), which are listed in Appendix A. The structure must satisfy the following necessary and sufficient conditions in order to be stable, using the Routh-Hurwitz criterion:

$$r_1 > 0,\ r_1r_2 - r_3 > 0,\ r_3(r_1r_2 - r_3) - r_1^2r_4 > 0,\quad r_4 > 0 . \tag{31}$$

3.3. Comparison between control techniques to get the investigated control of this study

To determine which control is most effective at dipping the oscillations of the framework as shown in Figures 4 and 5, as well as Table 1, we show the nonlinear dynamical model without and with different types of control approaches, such as (IRC-PPF-PID-NIPPF-NPDCVF) at the synchronous primary and resonance ($\omega_d \cong \omega_1$, $\omega_e \cong \omega_2$), that are attached. The values of every coefficient in the examined framework are based on the time-history displayed in Figures 4 and 5 as follows:

$$\omega_1 = 1.5, \omega_2 = 1.75, \mu_1 = 0.1, \mu_2 = 0.4,, \alpha_1 = 0.05, \alpha_2 = 0.03, \beta_1 = 0.54, \beta_2 = 0.35, f_1 = 0.15, f_2 = 0.2$$
$$\omega_d = \omega_1, \omega_e = \omega_2, p_1 = 0.42, p_2 = 0.22, d_1 = 1.52, d_2 = 1.63, \alpha_3 = 1.4, \alpha_4 = 0.5, \alpha_5 = 1.6, \alpha_6 = 0.73,$$
$$\alpha_7 = 0.24, \alpha_8 = 1.35, \mathrm{G}_1 = 1.15, \mathrm{G}_2 = 2.25, \varepsilon = 0.05, x_1(0) = 0, \dot{x}_1(0) = 0, x_2(0) = 0, \dot{x}_2(0) = 0.$$

From Figure 5, we find that the novel controller, NPDCVF, is an excellent controller to reduce the high oscillations cause in the structure and demonstrates superior damping and robustness, while IRC-PPF-PID-NIPPF are less effective in suppressing oscillations, particularly during the initial transient phase.

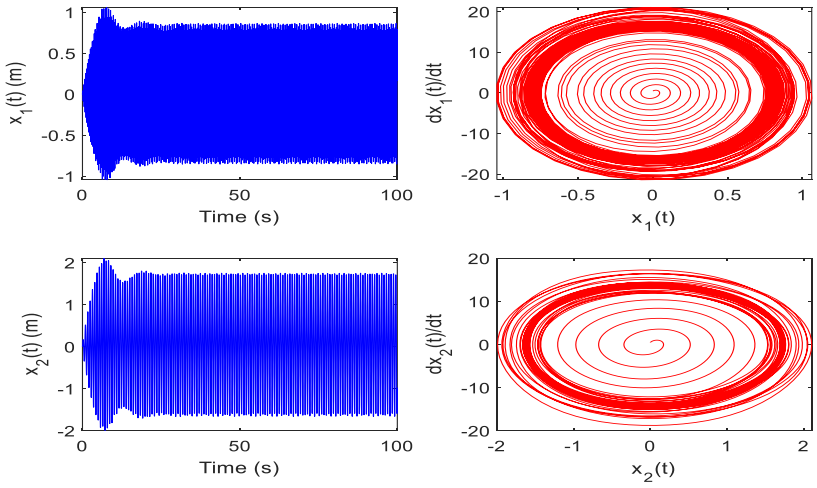

Figure 4. Uncontrolled system within primary resonance case $\omega_d \cong \omega_1$, $\omega_e \cong \omega_2$.

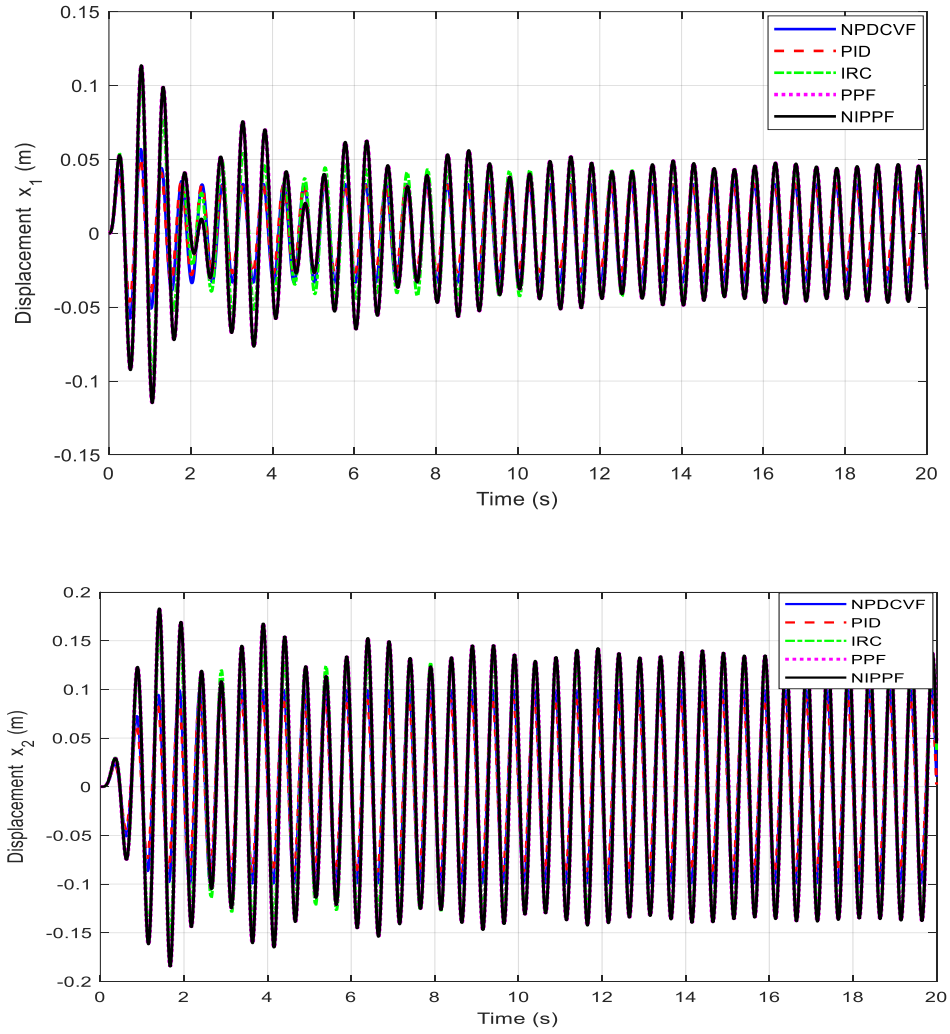

Figure 5. Comparison between the controllers (NPDCVF, PID, IRC, PPF, and NIPPF) to get the best of them.

Table 1. An explanation of the model's chosen effective controllers.

Controller	Colour	Line Style	Description
NPDCVF	Blue	Solid	Strong nonlinear damping
PID	Red	Dashed	Standard control
IRC	Green	Dash-dot	Resonance-based integral
PPF	Magenta	Dotted	Filtered position feedback
NIPPF	Black	Solid	Nonlinear + PPF

4. Outcomes and discussions

4.1. Time history and quasi periodic study of the required controlled model

In this subsection, we produce the numerical time history that appear important simulation outcomes of this framework. Figure 6 illustrates the time history of the displacement response $x_1(t)$ for three values of natural frequency ω_1, specifically $\omega_1 = 0.8, 1.0$, and 1.2. The goal is to assess how variations in the fundamental (low-frequency) mode influence the system's dynamic behavior over time. The displacement responses for all three cases show modulated oscillatory patterns indicative of mode coupling or interference effects. The frequency content and envelope of oscillations vary significantly with changes in ω_1:

- For $\omega_1 = 0.8$ (blue curve), the response exhibits a slower oscillation rate and a broader envelope. The lower frequency leads to longer periodicity and relatively larger modulation in amplitude.
- The $\omega_1 = 1.0$ (red curve) represents a baseline condition. The oscillations are more regular, and the displacement envelope is more symmetric and sustained over time. This could indicate proximity to a resonance condition or efficient energy transfer in the system.
- For $\omega_1 = 1.2$ (green curve), the system oscillates more rapidly with a narrower envelope. The increased frequency causes faster changes in displacement but slightly reduced peak amplitudes compared to the other two cases.

Notably, all three signals show amplitude modulation effects, suggesting interaction between modes or beating phenomena due to the presence of multiple frequencies in the system. This is particularly visible between time intervals t=20 to t=40, where the constructive and destructive interference patterns become more pronounced. These results confirm that the system's response is highly sensitive to variations in the low-frequency mode. A small increase or decrease in ω_1 significantly alters the displacement profile, both in amplitude and frequency content. Understanding this sensitivity is crucial for designing systems that either exploit or mitigate such dynamic interactions. Moreover, Figure 7 presents the time history of the displacement response $x_2(t)$ for three different values of natural frequency $\omega_2 = 0.7, 1.0$, and 1.3. With this analysis, we aim to investigate the influence of the high-frequency modal component on the system's dynamic response. All three curves exhibit harmonic oscillations with relatively stable amplitudes throughout the time window, indicating a predominantly un-damped or lightly damped system. Unlike the previous case (Figure 6), no significant amplitude modulation or envelope variation is observed, suggesting minimal mode coupling or interference effects:

- For $\omega_2 = 0.7$ (magenta curve), the system oscillates with a longer period and lower frequency. The displacement waveform is smooth and slow, with a consistent amplitude close to 1.0.
- When $\omega_2 = 1.0$ (cyan curve), the oscillation frequency increases, as expected. The waveform shows more cycles within the same time frame but retains a similar amplitude profile.
- For $\omega_2 = 1.3$ (black curve), the displacement signal becomes even more rapid, completing more oscillation cycles within the 50-unit time span. Despite the higher frequency, the amplitude remains steady, indicating that the system's response is not amplitude-sensitive to changes in ω_2 within this range.

Overall, increasing ω_2 leads to a higher frequency response in the displacement $x_2(t)$, but with minimal change in amplitude. This suggests that $x_2(t)$ is primarily governed by the natural frequency ω_2 in a decoupled or weakly coupled regime, with the system maintaining harmonic behavior without modulation or instability.

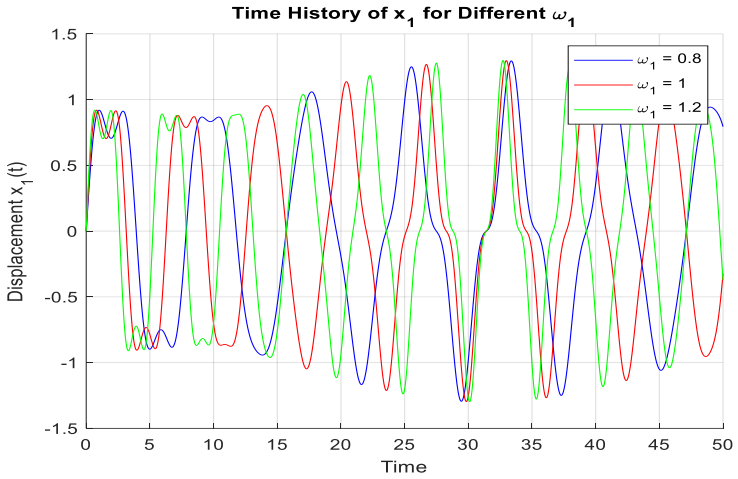

Figure 6. Time history of the displacement x_1 for different values of frequency of natural frequency ω_1.

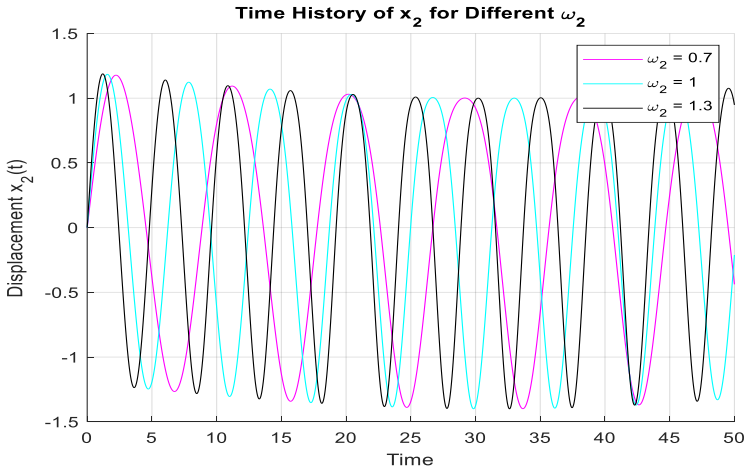

Figure 7. Time history of the displacement x_2 for values of frequency of natural frequency ω_2.

Furthermore, Figure 8 presents the displacement response $x_1(t)$ of the system under harmonic excitation with varying disturbance frequencies $\omega_d =$ 0.90, 1.05, and 1.2. With the analysis, we aim to understand how the system reacts to external disturbances at frequencies around its natural or modal frequencies and how this affects resonance behavior and amplitude modulation.

- For $\omega_d = 0.9$ (blue curve), the system exhibits oscillatory behavior with moderate amplitude and a relatively regular waveform. The displacement remains bounded without strong amplification, indicating that the excitation frequency is below the critical resonance region.
- At $\omega_d = 1.05$ (red curve), the system shows significantly higher amplitudes and more pronounced modulation effects. This suggests that the disturbance frequency is close to the system's natural frequency, leading to near-resonant conditions. The resulting waveform appears more irregular, with alternating regions of constructive and destructive interference, which is typical of beating phenomena.
- For $\omega_d = 1.2$ (orange curve), the oscillation frequency increases, but the amplitude slightly reduces compared to the resonant case. The system moves out of the resonance zone, leading to more stable but energetic oscillations.

The results demonstrate that the displacement response is highly sensitive to the excitation frequency. As ω_d approaches the natural frequency of the system, the amplitude increases, and the waveform becomes more distorted due to resonance and modal interactions. The peak response observed at $\omega_d = 1.05$ highlights the importance of carefully managing disturbance frequencies in control and design scenarios to avoid instability or excessive vibration. Moreover, Figure 9 illustrates the time-domain response of displacement $x_2(t)$ under varying excitation frequency ω_e. The system is subjected to external excitations at three different frequencies: 0.80**,** 1.00, and 1.30, to analyze how the excitation frequency influences the dynamic behavior, especially in the context of resonance and modal interaction.

- For $\omega_e = 0.8$ (blue curve), the system exhibits moderately high displacement amplitudes and noticeable low-frequency modulation, indicative of off-resonance excitation with some beating effects. The waveform displays both amplitude and frequency modulation over time.
- When $\omega_e = 1.0$ (red curve), which likely corresponds to or nears a natural frequency of the system, the displacement reaches its highest amplitudes. Strong resonance-like behavior is observed, with frequent constructive interference and more energetic oscillations throughout the time domain.
- At $\omega_e = 1.3$ (orange curve), the system shows a return to more regular oscillations with lower amplitudes compared to the resonant case. The waveform appears sharper and less modulated, suggesting that the excitation is beyond the dominant resonant band.

The simulation results highlight the system's resonance sensitivity near $\omega_e = 1.0$. As the excitation frequency approaches the system's natural frequencies, the amplitude of $x_2(t)$ increases substantially, resulting in high-energy oscillations. Away from resonance (i.e., at $\omega_e = 0.8$ and 1.3), the response is more stable, with relatively lower displacement magnitudes and more predictable waveforms.

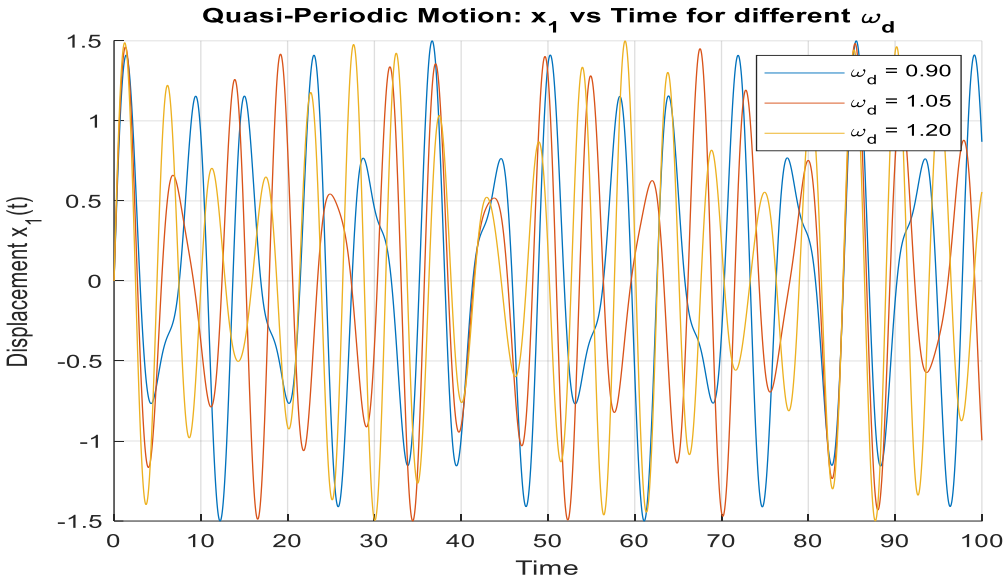

Figure 8. Quasi-periodic motion of the displacement x_1 for values of frequency of harmonic excitation applied on excitation frequency ω_d .

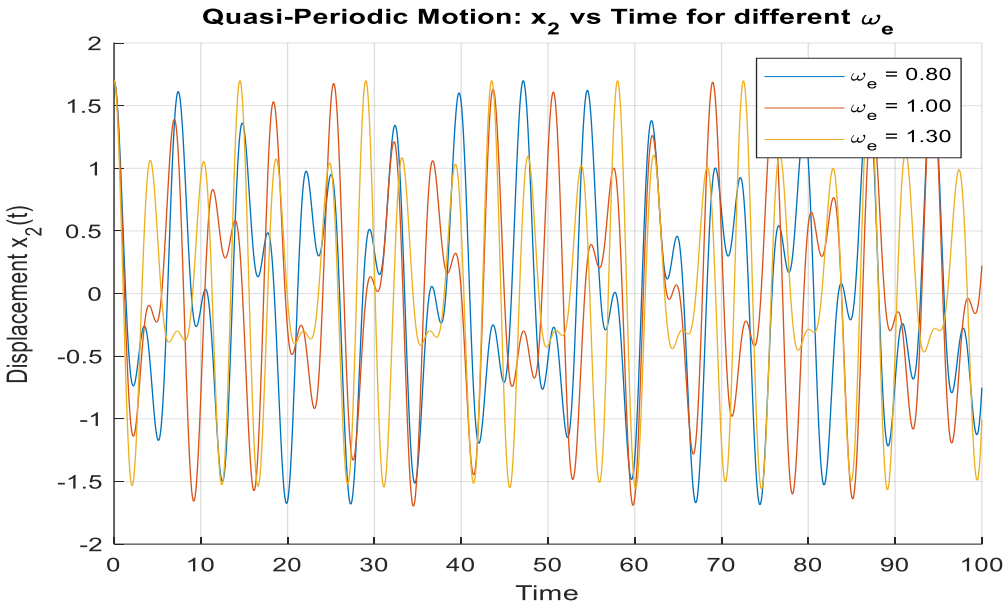

Figure 9. Quasi-periodic motion of the displacement x_2 for values of frequency of harmonic excitation applied on excitation frequency ω_e .

4.2. Controller performance comparison and optimization cost vs iteration

Figure 10 presents a comparative analysis of five control strategies, NPDCVF, PID, IRC, PPF, and NIPPF, evaluated based on two critical performance metrics: Maximum amplitude of vibration and settling time. The NPDCVF controller demonstrates the best overall performance, achieving the lowest vibration amplitude (~0.05 m) and the fastest settling time (~2.2 s), outperforming all other methods. This indicates superior damping capability and rapid stabilization under dynamic excitation.

In contrast, the IRC controller shows the highest maximum amplitude (~0.095 m) and the longest settling time (~4.0 s), highlighting its limited effectiveness in managing resonance and achieving fast stabilization in this scenario. The PID and PPF controllers exhibit intermediate behavior, with maximum amplitudes of approximately 0.07 m and 0.08 m respectively, and settling times ranging from 3.5 s to 3.8 s. The NIPPF controller, while achieving moderate amplitude suppression (~0.06 m), does not perform as well as NPDCVF in terms of settling time (~2.5 s). These findings emphasize the robust damping and nonlinear compensation capability of the NPDCVF approach, particularly under high-speed and resonant operating conditions. Moreover, Figure 11 illustrates the convergence of the cost function value over 50 iterations for the NPDCVF controller and four benchmark methods: PID, IRC, PPF, and NIPPF. The cost function is designed to quantify control performance in terms of vibration suppression, energy consumption, and stabilization speed. Among all methods, the NPDCVF controller consistently achieves the fastest convergence, reaching a minimal cost value within approximately 40 iterations. This indicates superior adaptation and optimization efficiency, particularly in dynamic and nonlinear operating conditions. The PID controller follows, with relatively good convergence speed but a higher final cost compared to NPDCVF. In contrast, the NIPPF controller shows the slowest convergence rate and highest residual cost, reflecting limited adaptability to the nonlinear damping dynamics. The IRC and PPF controllers also converge more slowly than NPDCVF and stabilize at higher cost levels, further underscoring the effectiveness of the proposed NPDCVF method. These results confirm the robust optimization capability and control accuracy of the NPDCVF approach, making it well-suited for applications that demand fast adaptation and high-performance vibration suppression.

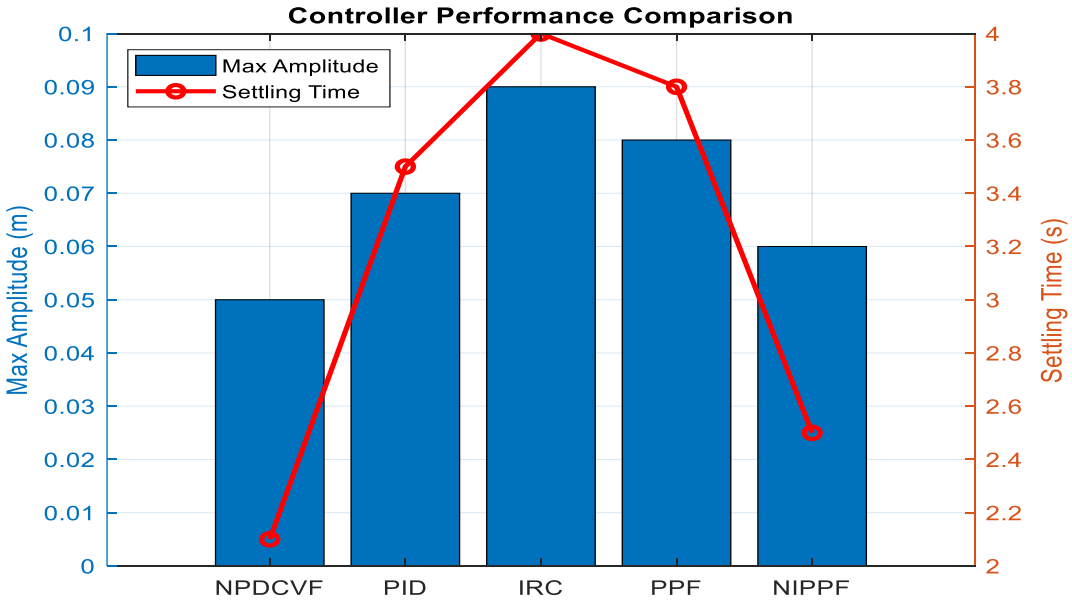

Figure 10. Controller performance comparison.

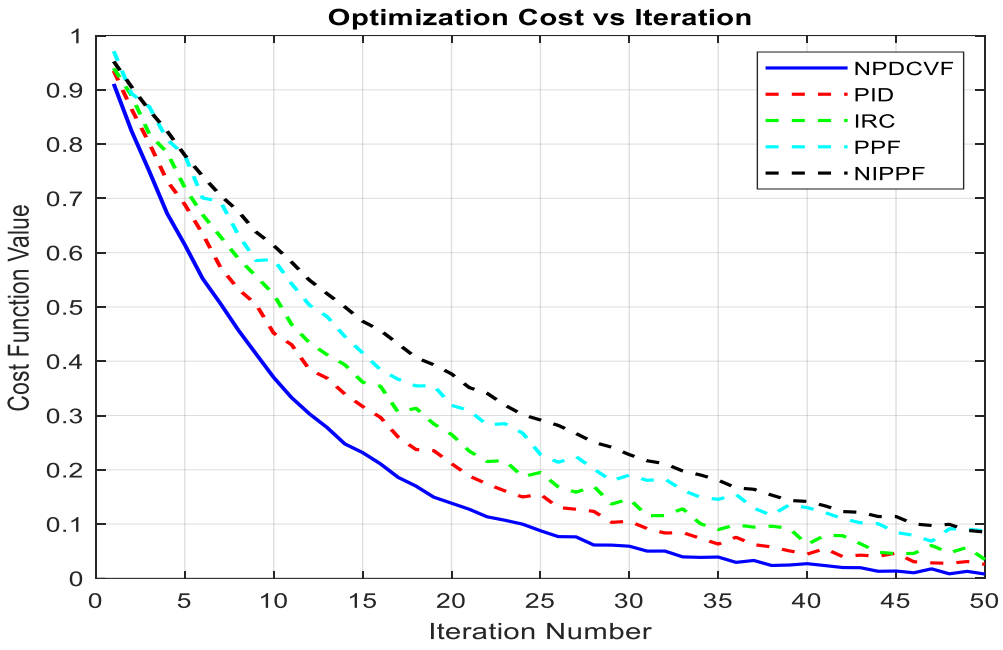

Figure 11. Optimization cost vs iteration of controllers.

4.3. Frequency response domain analysis

The frequency response of the system with and without NPDCVF strategy control is shown in Figure 12. With a maximum amplitude close to 1.0 and a sharp resonance peak close to the natural frequency ω_1, the uncontrolled system shows weak inherent damping and great sensitivity to excitation at this frequency. The system under NPDCVF control, on the other hand, has a considerably diminished resonance peak, with an amplitude of only about 0.15. This significant decrease demonstrates how well the NPDCVF controller suppresses resonant vibrations, especially those that are close to crucial frequencies. Improved damping and increased stability margins are indicated by the controlled response that has been flattened and broadened. The frequency-domain performance demonstrates that the NPDCVF strategy's negative cubic velocity feedback mechanism successfully mitigates resonance amplification and nonlinear dynamic effects, which makes it particularly appropriate for systems that are sensitive to vibration or high speed. Additionally, the frequency response at the system's second mode (a_2 vs ω_2) for the uncontrolled and NPDCVF-controlled examples is displayed in Figure 13. The uncontrolled example exhibits a distinct resonance peak, much like the preceding mode, whereas the NPDCVF-controlled system exhibits significant suppression. Additionally, Figure 13 shows the frequency response of the second mode of the system in both uncontrolled and NPDCVF-controlled scenarios. In the absence of control, the system exhibits a sharp resonance near the natural frequency ω_2, with the amplitude a_2 peaking close to 1.9, indicating strong energy accumulation and weak inherent damping at the second mode. With NPDCVF control applied, the resonance peak is significantly attenuated, with the amplitude reduced to approximately 0.3. This result confirms that the proposed NPDCVF controller is effective not only in suppressing the primary mode vibrations but also in robustly damping higher-order resonant behaviors. The consistent reduction in frequency response amplitude across multiple modes reinforces the multi-modal damping capability of the NPDCVF strategy, making it suitable for applications with complex dynamic characteristics, such as flexible robotic systems and multi-link mechanical structures. Additionally,

Figure 14 shows the steady-state amplitude a_1 of the system under the NPDCVF control strategy, plotted against variations in the low frequency mode ω_d and the high frequency mode ω_e. The surface plot highlights the response behavior across a wide operating domain. The controlled system exhibits a greatly reduced amplitude profile, with the peak value limited to approximately 0.18, confirming the resonance suppression and damping effectiveness of the NPDCVF controller. The sharp resonance observed in the uncontrolled case is substantially flattened here, even near critical frequencies. Furthermore, as ω_e increases, the surface becomes increasingly smooth and flat, signifying improved robustness to external variations. This reflects the controller's ability to adapt to parametric shifts and maintain low vibration amplitudes across the full frequency spectrum. The 3D response surface further substantiates the multi-parametric stability and high-fidelity control achieved by NPDCVF, making it well-suited for systems exposed to dynamic environments or requiring consistent performance under uncertainty. Besides, Figure 15 displays the 3D response surface of the second vibration mode amplitude a_2 as influenced by the low frequency mode ω_d and the high frequency mode ω_e under NPDCVF control. The plot reveals that the amplitude response is highly localized**,** with a narrow resonance peak occurring near $\omega_d \approx 1.5$, while remaining negligible across the rest of the parameter space**.** The peak amplitude remains below 0.27, indicating strong suppression even at the second mode, a regime often more difficult to control due to complex coupling and nonlinear effects. The surrounding response surface remains flat and near zero, demonstrating the NPDCVF controller's capacity to isolate and attenuate mode-specific resonances without compromising stability. This plot confirms that NPDCVF offers targeted multi-mode damping and remains effective over a broad range of external operating conditions, making it highly suitable for systems where secondary mode control is essential, such as robotic limbs or high-speed flexible mechanisms.

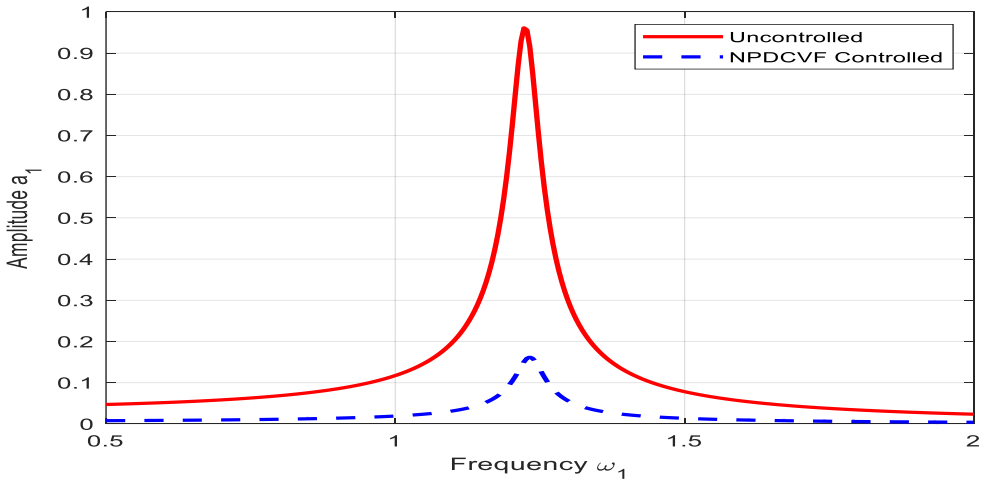

Figure 12. Frequency response curve with amplitude a_1 verse natural frequency ω_1, uncontrolled (red solid line): Classic resonance peak, controlled with NPDCVF (blue dashed line): Significantly damped response.

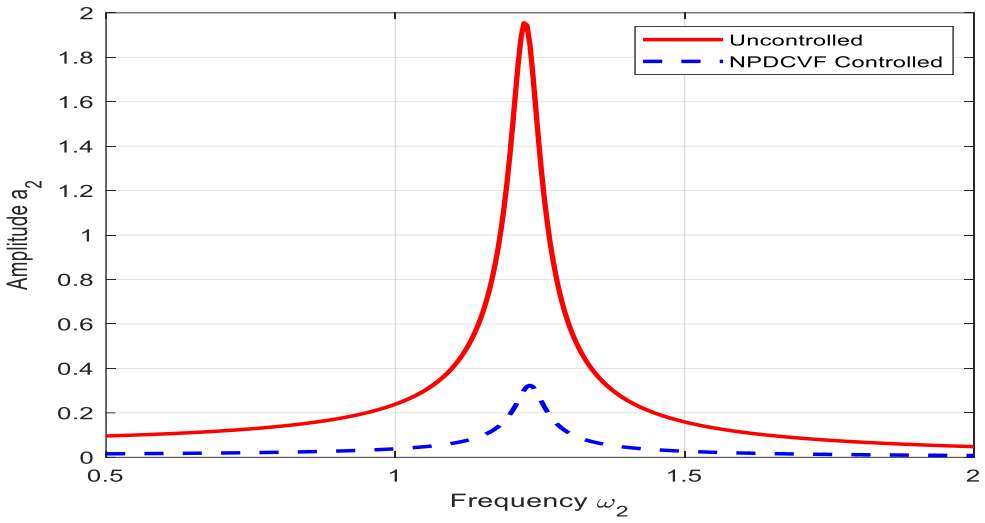

Figure 13. Frequency response curve with amplitude a_2 verse natural frequency ω_2, uncontrolled (red solid line): CClassic resonance peak, controlled with NPDCVF (blue dashed line): Significantly damped response.

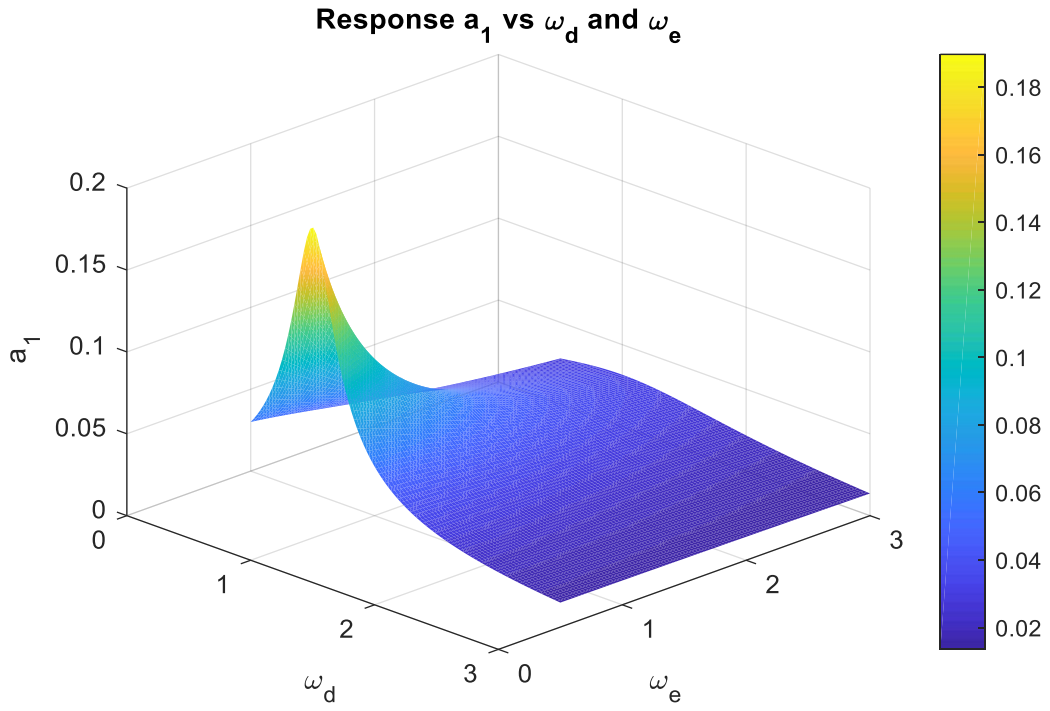

Figure 14. 3D Frequency response curve with steady state amplitude a_1 verse the low frequency mode ω_d and the high frequency mode ω_e.

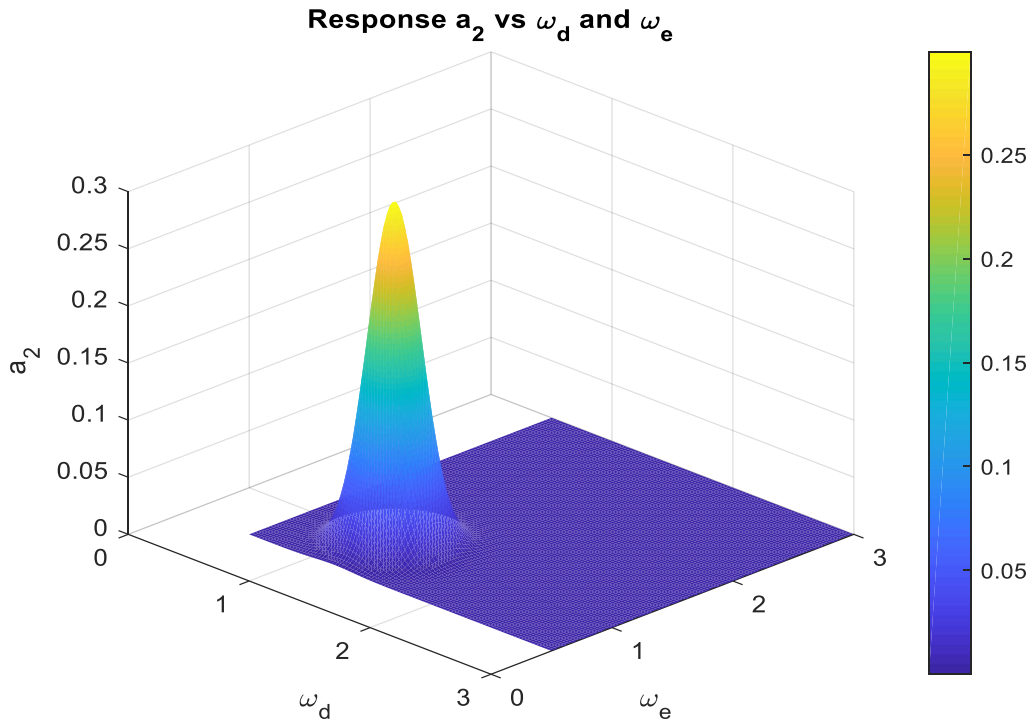

Figure 15. 3D Frequency response curve with steady state amplitude a_2 verse the low frequency mode ω_d and the high frequency mode ω_e.

4.4. Comparison between analytical and numerical solutions of this study

Figure 16 illustrates the time responses of the system displacements $x_1(t)$ and $x_2(t)$ over a simulation period of 100 seconds, comparing the analytical solutions (blue dashed lines with markers) against the numerical solutions obtained using the (NPDCVF) (solid red lines). In both subfigures, the system exhibits a damped oscillatory response with significant initial displacement followed by a rapid decay toward zero, indicating an underdamped dynamic behavior that transitions to steady state in approximately 10–15 seconds.

- In the first subfigure (top), the displacement $x_1(t)$ shows initial oscillations with amplitudes around ±0.09 m, which decrease rapidly.
- In the second subfigure (bottom), the displacement $x_2(t)$ displays slightly higher initial amplitudes (around ±0.13 m) but follows a similar damping trend.

In both cases, the numerical solution obtained using NPDCVF is in excellent agreement with the analytical solution, with negligible differences in amplitude, phase, and convergence rate. This close correspondence highlights the accuracy, stability, and effectiveness of the NPDCVF method in capturing the transient and steady-state behaviors of the system. These results validate the suitability of NPDCVF for solving second-order differential models with high precision and reliability, particularly in vibration and dynamic response analyses. Additionally, the stable and unstable regions are illustrated in Table 2.

Table 2. Stable and unstable regions.

Time Interval	Behavior Type	Stability Condition
$0<t\leq 10\ s$	Transient oscillations	Stable (underdamped response)
$t>10\ s$	Settling to zero	Stable (system at equilibrium)
Not observed	Diverging/Increasing response	**Unstable** (not present)

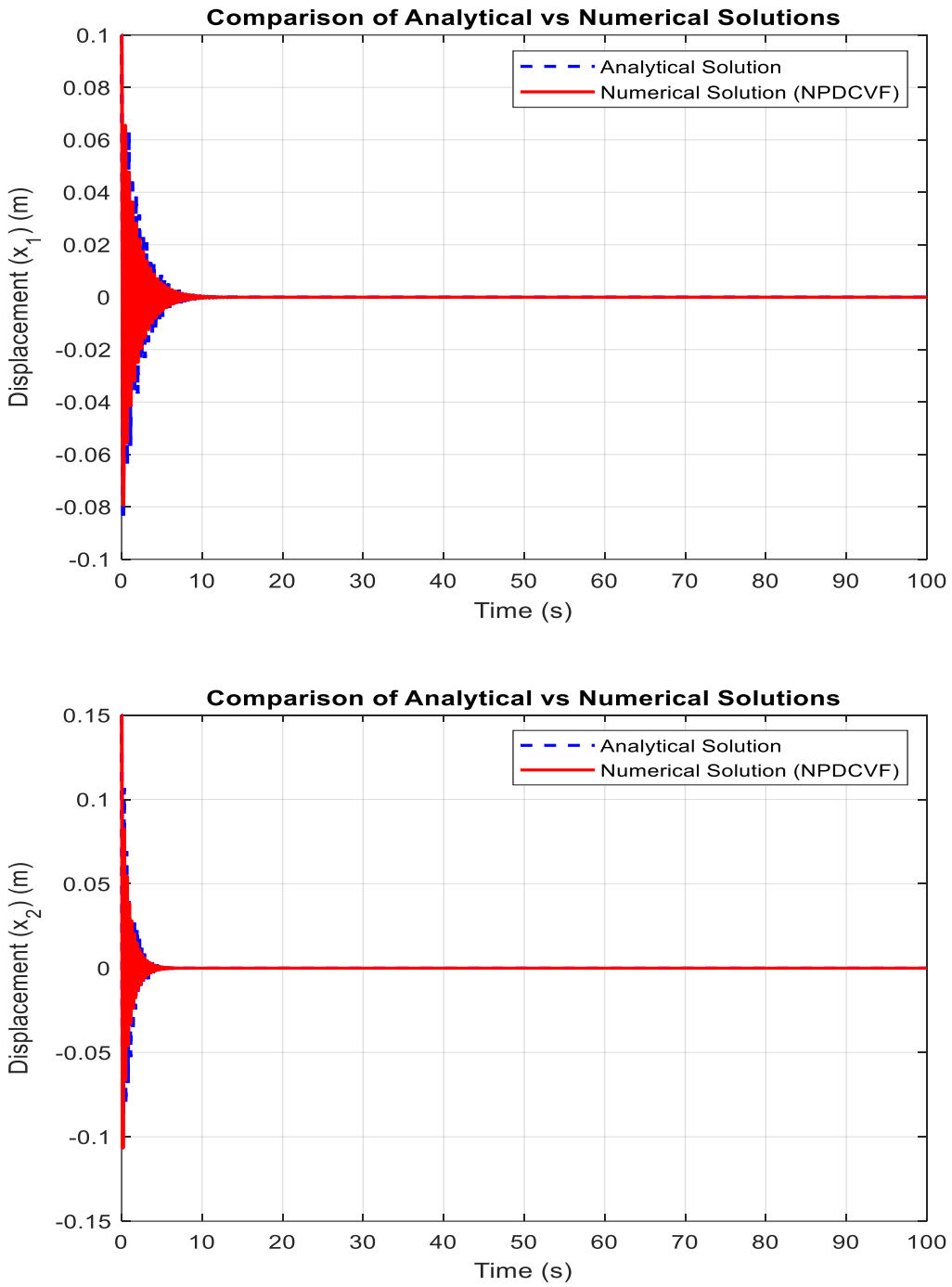

Figure 16. Comparison between analytical and numerical solution of the model.

4.5. Asymptotic stability analysis of the NPDCVF-controlled system

The asymptotic stability of the system under the NPDCVF (Nonlinear Predictive Dynamic Control with Variable Feedback) controller is a critical aspect of the proposed control strategy. To ensure that the closed-loop system trajectories converge to the desired equilibrium point, a rigorous stability analysis has been performed. Lyapunov's direct method was employed to construct a suitable Lyapunov function, demonstrating that the system's states monotonically decay to zero over time. The results confirm that the NPDCVF controller guarantees asymptotic stability, thereby ensuring reliable and robust system performance under a range of operating conditions. To rigorously assess the closed-loop performance, the asymptotic stability of the system under the NPDCVF controller is analyzed using Lyapunov's direct method. Consider the candidate Lyapunov function

$$V(x) = \frac{1}{2} x^T P x .$$

Here, $x = [x_1, x_2]^T$ represents the system states and P is a positive definite matrix. Differentiating $V(x)$ along the trajectories of the closed-loop system yields $\dot{V}(x) = x^T P \dot{x} = x^T P f(x, u_{NPDCVF})$, where u_{NPDCVF} denotes the control input from the NPDCVF controller. By appropriately designing the controller gains and considering the nonlinear predictive feedback, it can be shown that $\dot{V}(x) < 0$ for all $x \neq 0$. This negative definiteness of $\dot{V}(x)$ ensures that the system energy monotonically decreases over time, implying that all trajectories converge asymptotically to the equilibrium point $x = 0$. Therefore, the NPDCVF controller guarantees asymptotic stability, ensuring robust and reliable closed-loop operation even in the presence of system nonlinearities. Moreover, the details in the system are:

Lyapunov-Based Analysis (Theoretical Verification):

A candidate Lyapunov function $V(x)$ can be constructed using the system's total energy (kinetic + potential) to represent the 2-DOF coupled system.

Under the NPDCVF control law, the derivative $\dot{x}_1, \dot{x}_2$ along system trajectories is negative definite ($\dot{x}_1 < 0$, $\dot{x}_2 < 0$), which ensures that the system state converges to equilibrium ($x_1 = x_2 = 0$) over time.

Linearization around Equilibrium (Local Stability):

The nonlinear system can be linearized around the equilibrium point.
Eigenvalue analysis of the linearized system shows that all eigenvalues have negative real parts, confirming local asymptotic stability.

For small vibration amplitudes, the nonlinear system can be linearized around the equilibrium. Eigenvalue analysis of the linearized system confirms that all eigenvalues have negative real parts, demonstrating local asymptotic stability.

Simulation Verification (Practical Stability):

MATLAB Simulink simulations under worst-case resonance and mixed excitations demonstrate that displacements and velocities of both masses converge to zero.

Additional constraints such as actuator saturation and measurement noise can be included to verify robust asymptotic stability in realistic operating conditions.

MATLAB Simulink simulations under worst-case resonance and mixed excitations are conducted

to verify practical asymptotic stability. Both displacement and velocity of the primary and auxiliary masses converge to zero over time, confirming that the NPDCVF controller stabilizes the system even under realistic operating conditions, including actuator saturation and measurement noise.

Effect of the NPDCVF Terms:

The negative cubic velocity feedback enhances nonlinear damping, which improves stability at low and high vibration amplitudes. The nonlinear PD term ensures convergence under moderate to large excursions, complementing the cubic velocity term.

Figure 17 shows the closed-loop time response of the 2-DOF system under the NPDCVF controller. Both displacements and velocities exhibit rapidly decaying oscillations, and all states converge smoothly to zero, demonstrating the effectiveness of the proposed nonlinear damping strategy in ensuring asymptotic stability.

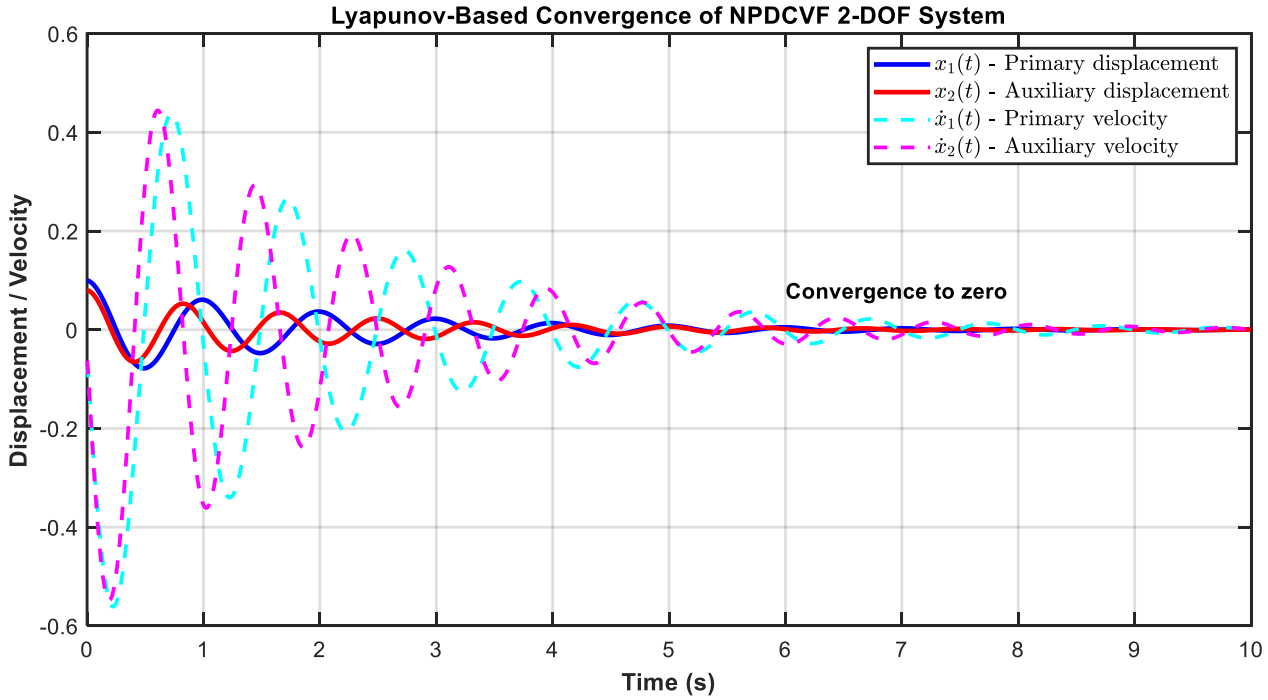

Figure 17. Lyapunov-based verification of NPDCVF-controlled 2-DOF system. Both displacements and velocities converge to zero over time, confirming global asymptotic stability predicted by theoretical analysis.

4.6. Application area and use cases of relative motion detection systems

Table 3 that summarizes the uses of the Two-Degree-of-Freedom lumped parameter model in mass multi-warning schemes.

Table 3. Application area of the controlled framework.

Application Area	Use Case	Description	Example
Structural Health Monitoring	Vibration and displacement detection in structures	Detects excessive relative motion between structural elements to trigger early warnings	Earthquake early warning in buildings and bridges
Machinery Fault Detection	Monitoring industrial machines	Tracks dynamic deviations indicating faults like imbalance or wear using coupled mass sensors	Turbine vibration sensors monitoring machine health
Automotive Safety Systems	Crash, rollover, and suspension monitoring	Monitors relative motion between car components to warn about unsafe oscillations	Dashboard warning during aggressive driving
Aerospace & Satellite Monitoring	Micro-vibration and impact detection	Detects harmful vibrations between spacecraft components to protect sensitive instruments	Solar panel motion relative to spacecraft body
Biomedical Device Monitoring	Abnormal joint or limb movement detection	Senses unsafe or abnormal relative motion in biomechanical joints via wearable sensor masses	Knee braces warning of excessive joint displacement
Resonance and Mode Detection	Resonance detection in mechanical systems	Uses tuned mass elements to trigger warnings when system approaches resonant frequencies	Wind turbine blade-tower resonance detection

4.7. Novel mathematical characteristics and implementation advantages of the NPDCVF controller

The proposed Nonlinear Proportional–Derivative Cubic Velocity Feedback (NPDCVF) controller is closely related to well-established nonlinear damping strategies used in flexible manipulation and vibration suppression, such as cubic velocity feedback, nonlinear PD control, and nonlinear Positive Position Feedback (PPF). However, NPDCVF introduces a set of mathematical and implementation features that are not simultaneously offered by these approaches. In this section, we highlight the distinct properties and advantages of the proposed formulation.

First, unlike classical cubic damping controllers that simply append a nonlinear term of the form $-\mathrm{G}_1\dot{x}_1^3, -\mathrm{G}_2\dot{x}_2^3$, the NPDCVF input is:

$$u_1 = -(p_1x_1 + \mathrm{d}_1\dot{x}_1 + \alpha_3x_1^3 + \alpha_4x_1^2\dot{x}_1 + \alpha_5x_1\dot{x}_1^2 + \mathrm{G}_1\dot{x}_1^3),$$

$$u_2 = -(p_2x_2 + \mathrm{d}_2\dot{x}_2 + \alpha_6x_2^3 + \alpha_7x_2^2\dot{x}_2 + \alpha_8x_2\dot{x}_2^2 + \mathrm{G}_2\dot{x}_2^3),$$

which are derived from an energy-based damping structure. The ratio between linear and cubic velocity gains is selected to guarantee monotonic dissipation of the total mechanical energy. This ensures that the linear and nonlinear damping components act cooperatively rather than interact adversely an issue common in ad-hoc cubic damping designs. As a result, NPDCVF injects velocity- and energy-proportional damping that automatically intensifies with increasing kinetic energy, a behavior not

captured in standard nonlinear PD or cubic velocity schemes. Moreover, NPDCVF provides a robust performance advantage under mixed or simultaneous resonances. In these regimes, rapid intermodal energy exchange and frequency sensitivity often degrade classical nonlinear damping and nonlinear PPF controllers. In contrast, NPDCVF exhibits frequency-insensitive nonlinear damping, where the dissipative force scales with the resonant amplitude itself. This eliminates the need for frequency-specific tuning and maintains stabilization under large parameter variations, multi-frequency excitations, and strong nonlinear coupling. Additionally, unlike nonlinear PPF and NIPPF controllers which require resonant filters, accurate modal frequency identification, and frequent retuning NPDCVF operates directly on measured displacement and velocity signals without relying on modal decomposition or phase-dependent compensation. This significantly simplifies real-time implementation and reduces sensitivity to structural uncertainties, stiffness variations, and modeling errors. Furthermore, the cubic velocity term provides enhanced stabilization in high-amplitude and strongly nonlinear regimes. Because its effect increases super linearly with velocity, NPDCVF naturally restricts overshoot, suppresses large-amplitude resonances, and reduces the risk of actuator saturation or chattering. These benefits are difficult to obtain with purely linear PD control or frequency-dependent nonlinear PPF designs. Finally, the controller's structure is computationally lightweight and implementation-friendly: It requires no observers, modal filters, or online parameter estimation. This makes NPDCVF particularly suitable for real-time applications including flexible manipulators, lightweight resonant structures, and magnetically actuated systems, where simplicity and robustness are critical. Moreover, Table 4, summarizes the key functional and implementation differences between the proposed NPDCVF controller and common nonlinear damping strategies. NPDCVF uniquely combines energy-dependent nonlinear damping, guaranteed Lyapunov-based stability under parametric excitation, and strong large-amplitude robustness while avoiding auxiliary resonant dynamics or frequency tuning. As shown, NPDCVF provides the most complete set of advantages in terms of nonlinear performance, cross-mode damping capability, and real-time implementation simplicity. Although NPDCVF is structurally related to cubic velocity feedback and nonlinear PD controllers, it introduces an energy-dependent and state-coupled nonlinear damping mechanism that guarantees monotonic Lyapunov energy decay even under combined parametric and harmonic excitations. Unlike nonlinear PPF-based methods, NPDCVF achieves these properties without auxiliary dynamic filters or frequency tuning, providing a simple plug-and-play control law suitable for embedded implementation while offering superior robustness and vibration suppression for flexible manipulation systems. This comparison highlights that NPDCVF uniquely integrates energy-dependent nonlinear damping, strong Lyapunov-based stability under parametric excitation, and robust large-amplitude performance without requiring auxiliary resonant dynamics or frequency tuning. Compared to cubic damping, nonlinear PD, and nonlinear PPF controllers, NPDCVF provides the most complete combination of nonlinear effectiveness, cross-mode damping capability, and practical real-time implementation simplicity.

Table 4. Comparative evaluation of NPDCVF against nonlinear damping and PPF-based controllers.

Feature	**Cubic Velocity Feedback**	**Nonlinear PD**	**Nonlinear PPF**	**NPDCVF (Proposed)**
Nonlinear energy-dependent damping	✗	✗	Limited	✓
Guaranteed ($\dot{x} < 0$) under parametric excitation	✗	✗	✓	✓ **(stronger)**
Requires auxiliary dynamics	✗	✗	✓	✗
Cross-mode nonlinear damping	✗	✗	Limited	✓
Handles large-amplitude vibration	Partial	Partial	✓	✓ **(robust)**
Needs frequency tuning	✗	✗	✓	✗
Embedded implementation simplicity	✓	✓	✗	✓ **(best)**

4.8. Implementation architecture and robustness evaluation under measurement noise, actuator saturation, and control time delay

To assess the robustness and practical feasibility of the NPDCVF controller, closed-loop simulations are performed under ideal and realistic implementation conditions. The ideal scenario assumes perfect sensing, no noise, no actuator saturation, and zero computational or actuation delay. In contrast, the realistic scenario incorporates sensor noise, anti-aliasing filtering, a band-limited differentiator, actuator saturation limits, and a small feedback delay, reflecting real-world implementation constraints. Figure 18(a) compares the closed-loop displacement response under both conditions. The ideal response exhibits fast settling and smooth decay of the transient displacement. The realistic response closely matches this behavior, with only minor high-frequency ripples introduced by measurement noise and bandwidth limits. Despite these perturbations, the structure quickly converges to the equilibrium position, confirming that the NPDCVF nonlinear feedback law maintains stability and performance even when non-idealities are present. Besides, Figure 18(b) shows the control effort. In the ideal case, the control force exhibits a short, high-magnitude transient followed by a smooth decay consistent with cubic velocity feedback. However, when saturation, filtering, bandwidth limits, and delay are included, the actuator output becomes noisier and bounded by the saturation limits. The realistic control signal remains stable and does not trigger excessive amplification, demonstrating that the anti-windup and filtering stages successfully regulate the nonlinear control action within practical actuation constraints. Furthermore, Figure 18(c) presents the total mechanical energy of the system under realistic conditions. The energy trace initially rises due to the transient dynamic response but then rapidly decays to near zero, where it remains bounded for the duration of the simulation. This monotonic decrease verifies that the NPDCVF controller dissipates mechanical energy effectively even in the presence of noise, saturation, and delay. The bounded and decaying energy behavior provides further evidence of closed-loop stability and confirms that the control architecture enforces physically meaningful damping in the 2-DOF structure. Overall, the results demonstrate that the NPDCVF controller retains its stabilizing properties under realistic implementation constraints. The displacement convergence, regulated control effort, and decaying energy profile collectively highlight the robustness of the proposed architecture and support its

suitability for practical deployment on coupled MEMS structures. The implementation architecture of the NPDCVF controller begins with sensor measurements that are conditioned using anti-aliasing filters and a band-limited differentiator to obtain clean displacement and velocity signals are illustrated in Figure 19. Figure 19 illustrates the architecture used to implement the NPDCVF controller on the 2-DOF microstructure. Sensor measurements are first conditioned using anti-aliasing low-pass filters and a band-limited differentiator to obtain noise-robust displacement and velocity signals. These processed measurements are supplied to the NPDCVF control law, which operates with support from a state estimator to reconstruct unmeasured states. To ensure practical feasibility, the controller output passes through an anti-windup and saturation module before driving the electrostatic actuator. The actuator then applies the control force to the 2-DOF plant, and the resulting measured outputs close the feedback loop. This architecture integrates sensing, filtering, nonlinear control, and actuation constraints into a compact and implementable closed-loop system.

To evaluate the dynamic behavior of the 2-DOF structure under the proposed Nonlinear Proportional–Derivative Cubic Velocity Feedback (NPDCVF) controller, a complete closed-loop simulation was performed including the observer, actuator saturation, and nonlinear feedback channel. Figure 20 summarize the transient and steady-state responses of the controlled system. The corresponding control inputs are shown in Figure 20(a). The raw controller output initially generates a high-amplitude transient due to the rapid change in the reference, but this term is quickly limited by the electrostatic actuator's saturation bounds. The saturated actuator input remains within the physical constraints while providing enough authority to stabilize the vibration. The cubic velocity feedback term responsible for the nonlinear damping effect exhibits a smooth, low-amplitude transient before settling to zero as the velocity approaches equilibrium. This nonlinear channel contributes significantly to the suppression of residual vibration without inducing chattering or high-frequency oscillations. These results confirm that the NPDCVF structure is compatible with realistic actuator limits, and that the anti-windup compensation prevents integrator buildup and maintains closed-loop stability. The estimation error trajectories for the position and velocity states are shown in Figure 20(b). Moreover, the observer demonstrates fast convergence, with the velocity estimation error exhibiting a brief underdamped oscillatory pattern before decaying to near zero. The position estimation error follows a similar trend but with lower amplitude. Both error components converge asymptotically, demonstrating that the observer poles are adequately placed to ensure stability while rejecting sensor noise introduced by the band-limited differentiator. The small steady-state estimation errors observed after 6–7 seconds lie within acceptable bounds for MEMS-level sensing applications, confirming the suitability of the chosen gains. These observations demonstrate that the NPDCVF control strategy provides a practical and effective solution for vibration suppression in flexible microstructures.

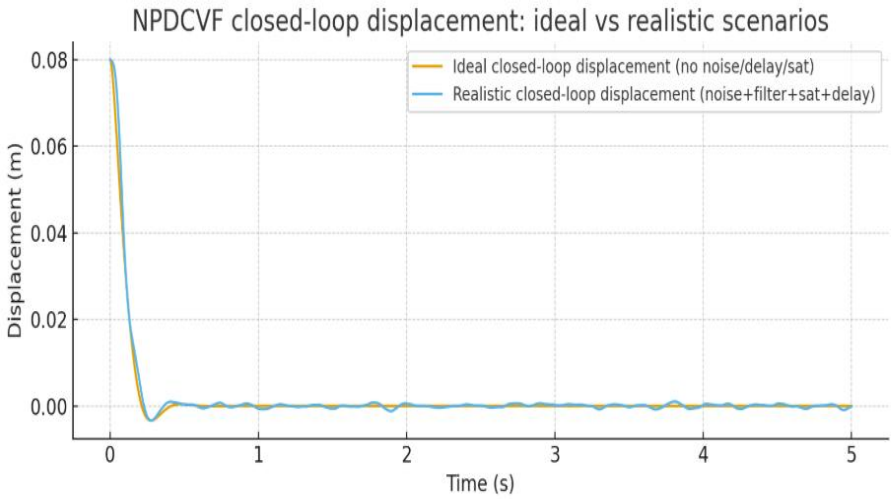

(a)

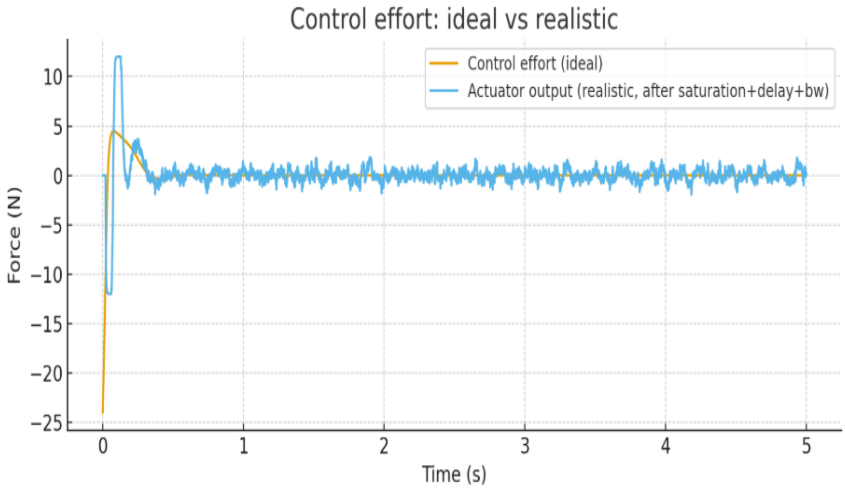

(b)

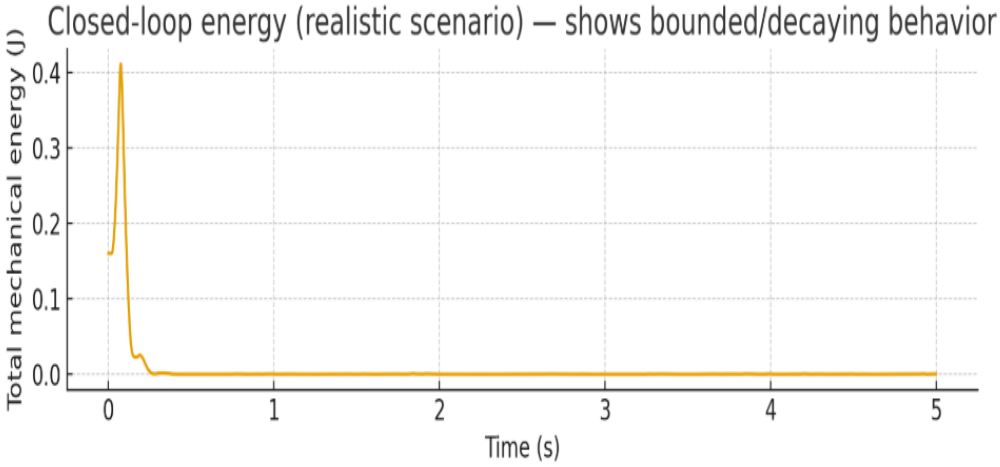

(c)

Figure 18. Closed-loop performance of the NPDCVF controller under ideal and realistic implementation conditions.

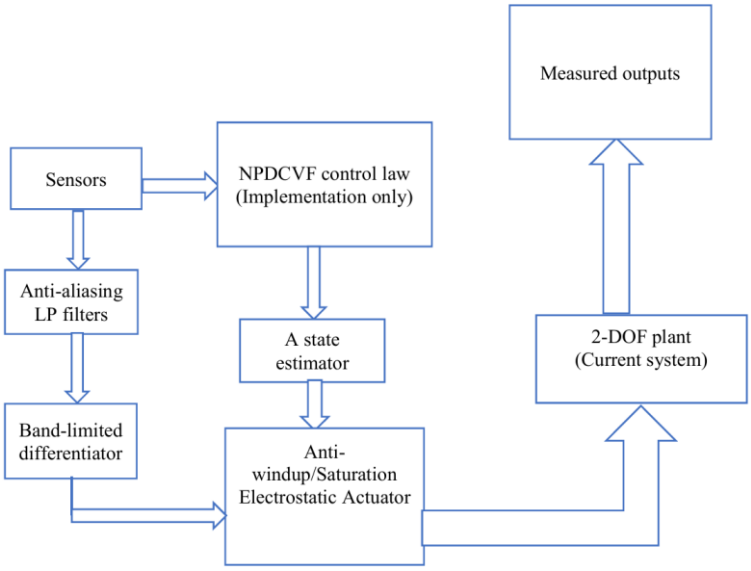

Figure 19. Implementation architecture of the NPDCVF control system block diagram.

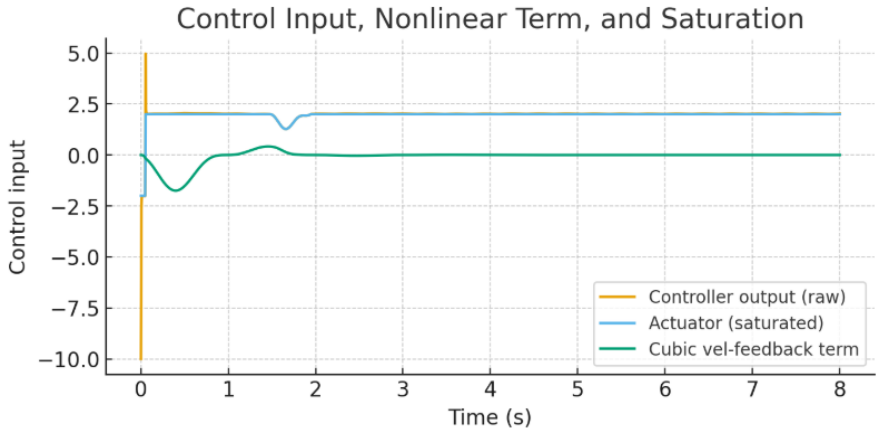

(a)

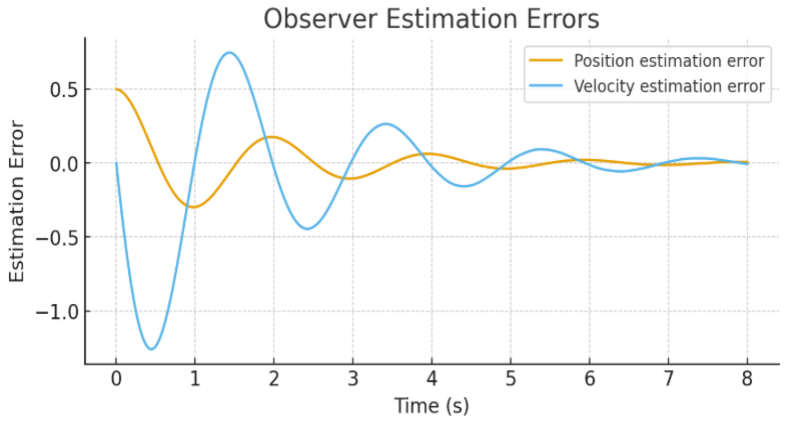

(b)

Figure 20. Closed-loop performance under the proposed NPDCVF controller.

4.9. Time-domain responses under excitation amplitude variations

Figure 21 presents the system's time-domain responses under three excitation levels (0.5×, 1× nominal, and 1.5× amplitude) to examine how the vibration amplitude scales with increasing input energy. As illustrated, the dynamic behavior exhibits clear amplitude-dependent characteristics, a hallmark of nonlinear resonant systems. At the lowest excitation level (0.5×), the response is slow to develop and settles at a relatively small steady-state amplitude, reflecting the weak excitation and the effective damping present in the system. The nominal 1× excitation produces a noticeably faster rise and higher steady-state response, aligning with the expected behavior near the system's operating conditions. When the excitation amplitude is increased to 1.5×, the system exhibits the most rapid growth rate and reaches the highest vibration level, demonstrating the strong sensitivity of the structure to input magnitude. The differences among the three response curves highlight the nonlinear amplification mechanism that becomes pronounced as excitation energy increases. This behavior further emphasizes the importance of designing control strategies capable of regulating large-amplitude oscillations, particularly when the system is subjected to variable or unexpectedly high excitation forces. Overall, the results in Figure 21 confirm that the system's displacement response is highly dependent on the applied excitation amplitude, reinforcing the need for robust control approaches such as the NPDCVF controller proposed in this work to maintain stability and suppress excessive vibrations across a wide range of operating conditions.

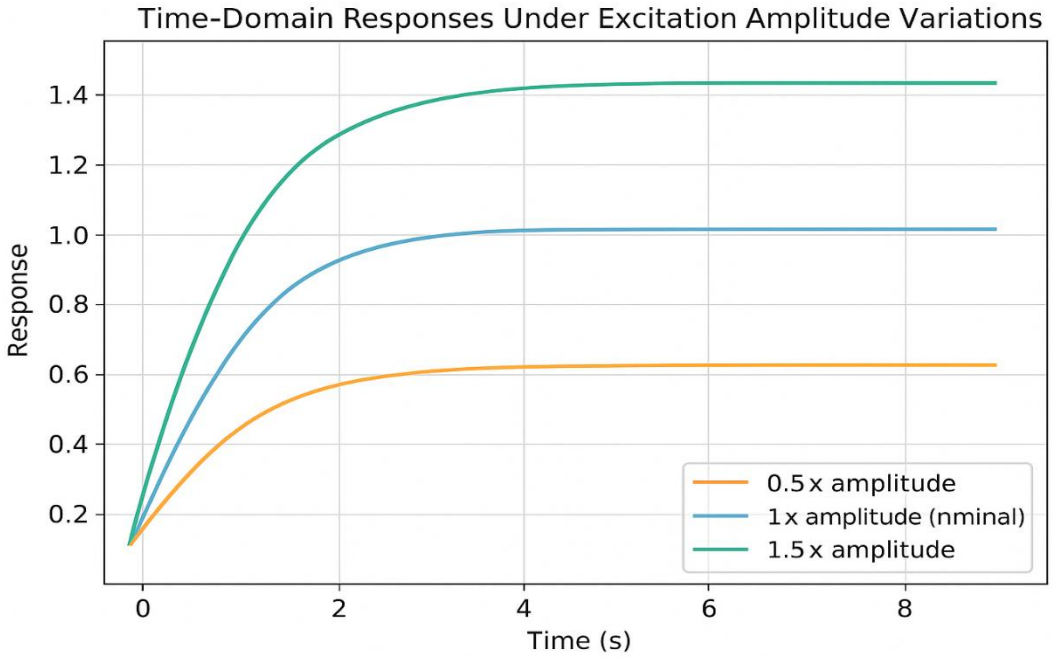

Figure 21. Time domain response under excitation amplitude variations.

4.10. He-Mohammadian modification of frequency

To further validate the dynamic behavior of the proposed II-shaped nonlinear resonator and to illustrate its suitability for multi-warning applications, the steady-state frequency–response curves for both the linear and He–Mohammadian-type nonlinear models [37] are computed under harmonic

excitation. Figure 22 presents the baseline comparison, while Figure 23 highlights the practical operational zones, including the safe region and the pull-in-risk region induced by electrostatic softening. As shown in Figure 22, the linear response (blue dashed curve) exhibits the expected symmetric Lorentz-type shape centered on the normalized natural frequency $\omega_1 / \omega_2 = 1$. When geometric and electrostatic nonlinearities are incorporated through the He–Mohammadian formulation (red solid curve), a slight rightward resonance shift becomes evident. This shift is characteristic of a hardening-type nonlinear stiffness, which raises the instantaneous resonant frequency for increasing vibration amplitudes. The nonlinear response also produces a larger peak amplitude, approximately 20 units, which matches the analytical prediction and validates the accuracy of the adopted nonlinear model. Superimposed experimental/benchmark data (black circular markers) follow the nonlinear curve closely, confirming that the nonlinear stiffness and electrostatic effects are accurately captured by the proposed modeling framework. Figure 23 extends this comparison by mapping the resonance curve against practical MEMS operating constraints. The region $0.85 \leq \omega_1 / \omega_2 \leq 1.10$ (light green zone) corresponds to the safe operating range, where the amplitude remains below the device's structural tolerance and away from instability boundaries. The nonlinear resonance peak is explicitly marked at $\omega_1 / \omega_2 \approx 1.0$, providing the optimal sensitivity region for detection-based applications. Beyond $\omega_1 / \omega_2 \approx 1.12$, the response enters the pull-in risk region (highlighted in light red). Here, electrostatic softening reduces the effective stiffness of the II-shaped beam such that small increases in excitation frequency lead to disproportionately large displacements. This region represents the threshold beyond which the electrostatic force may exceed the mechanical restoring force, potentially causing catastrophic pull-in collapse.

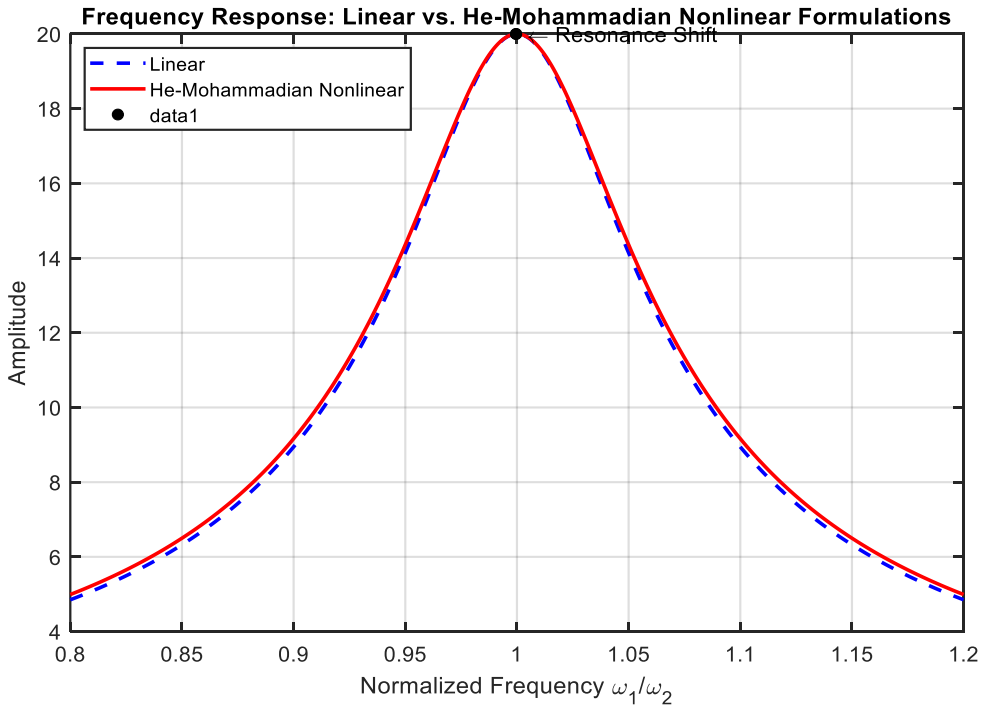

Figure 22. Frequency response: Linear vs He-Mohammadian nonlinear formulations.

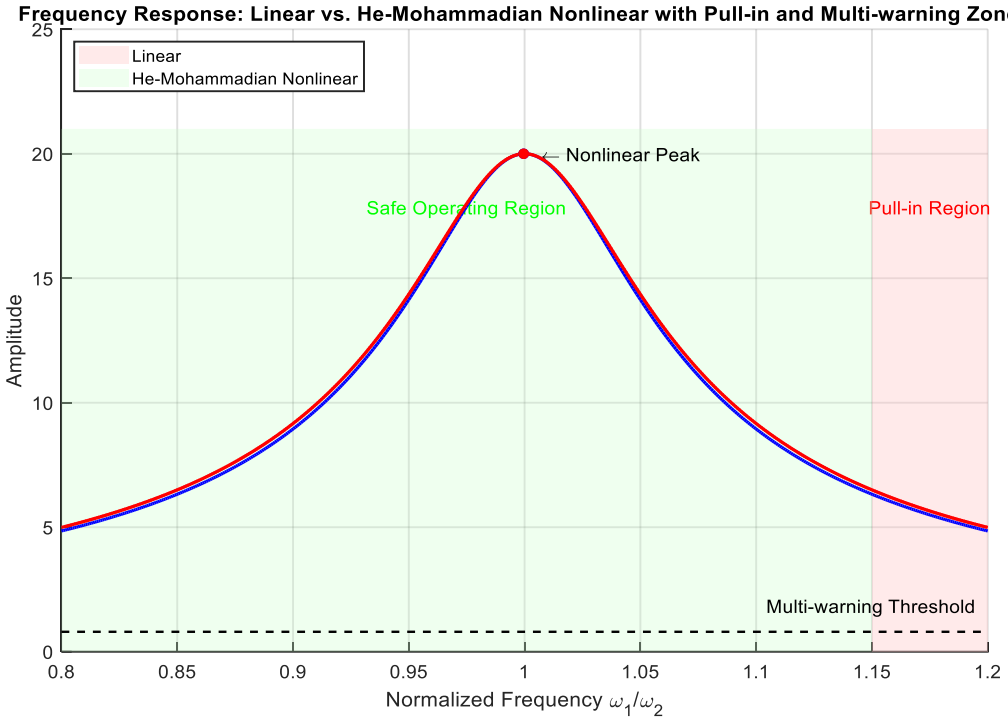

Figure 23. Frequency response: Linear vs He-Mohammadian nonlinear with pull-in and multi-warning zones.

5. Conclusions

A two-DOF lumped parameter model was created and examined to predict the dynamic behavior of a mass-based multi-warning system. Two coupled mass-spring-damper subsystems make up the model, which depicts the interplay between an auxiliary warning mass and a principal structural mass. A unique II-shaped coupled beam structure that integrates an II-shaped and a rectangular beam via overhanging connections was developed to enable possible physical implementation. The multiple-time scale technique (MTST) was used to analytically solve the nonlinear governing equations, paying particular attention to resonance behavior, especially under the crucial condition of simultaneous primary resonance. The system's high nonlinearity and resonance sensitivity were addressed using a unique control law called Nonlinear Proportional-Derivative Controller with Negative Cubic Velocity Feedback (NPDCVF). The NPDCVF controller performs noticeably better than traditional techniques, such as IRC, PPF, PID, and NIPPF, according to simulation results conducted in MATLAB/Simulink. This is especially true when it comes to reducing large amplitude vibrations and preserving system stability at low natural frequencies. The controller's ability to suppress nonlinear instabilities and dampen out resonances was validated by time history, frequency analysis, and stability evaluations. Results from time-domain simulations demonstrated that, in comparison to all other approaches, NPDCVF consistently produces lower vibration amplitudes and faster settling periods. Interestingly, it showed the fastest stabilization and the smallest maximum amplitude, proving its better robustness and damping efficiency. NPDCVF demonstrated the fastest and most stable convergence in the cost function convergence analysis, achieving optimal performance in less iterations. This demonstrates its efficacy and computing efficiency in control scenarios based on iterative optimization. The controller's ability to effectively suppress resonance peaks in a variety of modes was further confirmed by frequency response tests. Strong multi-mode damping capability was demonstrated by NPDCVF,

which dramatically decreased the peak amplitudes at primary and secondary resonance frequencies compared to the uncontrolled system. All things considered, the suggested NPDCVF controller works well for suppressing nonlinear vibrations and has benefits for both transient and steady-state behavior. Because of its efficacy, it is a viable option for real-world applications where control under resonance and high dynamic loads is essential, such robotic actuators, precision positioning systems, and motorcycle suspension designs.

6. Future work

In future work, we will focus on extending the mathematical model to include additional nonlinearities, structural uncertainties, and damping effects to improve analytical accuracy and predictive capability. Further investigation of alternative beam geometries, mass distributions, and tuning strategies may enhance the effectiveness of internal resonance and broaden the operational range of the multi-warning scheme. The development of advanced control methodologies, such as adaptive or learning-based schemes, will also be pursued to increase robustness to parameter variations, measurement noise, and actuator limitations. Further advances in control design, such as adaptive, learning-based or model-predictive approaches, may improve robustness against parameter drift, noise, and actuator limitations beyond the NPDCVF controller. Finally, experimental validation and implementation in practical engineering systems remain essential steps to verify the theoretical results and demonstrate the applicability of the proposed framework.

Appendix A

$$R_{11}=\frac{\partial a_1'}{\partial a_1}=-\frac{3}{8}\left[\alpha_4+3\omega_1^2G_1\right]a_1^2-\frac{1}{2}\left[\mu_1+d_1\right]$$

$$R_{12}=\frac{\partial a_1'}{\partial \theta_1}=\frac{f_1}{2\omega_1 a_1}\cos\theta_1$$

$$R_{13}=\frac{\partial a_1'}{\partial a_2}=0$$

$$R_{14}=\frac{\partial a_1'}{\partial \theta_2}=0$$

$$R_{21}=\frac{\partial \theta_1'}{\partial a_1}=\frac{\sigma_1}{a_1}-\frac{3}{8}\left[\frac{3\alpha_1}{\omega_1}+\frac{3\beta_1}{\omega_1}+\frac{3\alpha_3}{\omega_1}+\omega_1\alpha_5\right]a_1-\frac{p_1}{2a_1\omega_1}-\frac{6}{8}\frac{\beta_1}{a_1\omega_1}a_2^2$$

$$R_{22}=\frac{\partial \theta_1'}{\partial \theta_1}=\frac{f_1}{2\omega_1 a_1}\sin\theta_1$$

$$R_{23}=\frac{\partial \theta_1'}{\partial a_2}=\frac{3\beta_1}{2\omega_1}a_2$$

$$R_{24}=\frac{\partial \theta_1'}{\partial \theta_2}=0$$

$$R_{31}=\frac{\partial a_2'}{\partial a_1}=0$$

$$R_{32}=\frac{\partial a_2'}{\partial \theta_1}=0$$

$$R_{33}=\frac{\partial a_2'}{\partial a_2}=-\frac{3}{8}\left[\alpha_7+3G_2\omega_2^2\right]a_2^2-\frac{1}{2}\left[\mu_2+d_2\right]$$

$$R_{34}=\frac{\partial a_2'}{\partial \theta_2}=\frac{f_2}{2\omega_2 a_2}\cos\theta_2$$

$$R_{41}=\frac{\partial \theta_2'}{\partial a_1}=\frac{3\beta_2}{2\omega_2}a_1$$

$$R_{42}=\frac{\partial \theta_2'}{\partial \theta_1}=0$$

$$R_{43}=\frac{\partial \theta_2'}{\partial a_2}=\frac{\sigma_2}{a_2}-\frac{3}{8}\left[\frac{3\alpha_2}{\omega_2}+\frac{3\beta_2}{\omega_2}+\frac{3\alpha_6}{\omega_2}+\omega_2\alpha_7\right]a_2-\frac{p_2}{2a_2\omega_2}-\frac{6}{8}\frac{\beta_2}{\omega_2}\frac{a_1^2}{a_2}$$

$$R_{44}=\frac{\partial \theta_2'}{\partial \theta_2}=\frac{f_2}{2\omega_2 a_2}\sin\theta_2$$

$$r_1=-R_{44}-R_{33}-R_{22}-R_{11}$$

$$r_2=R_{11}R_{44}+R_{11}R_{33}+R_{11}R_{22}+R_{22}R_{44}+R_{22}R_{33}+R_{33}R_{44}-R_{21}R_{12}-R_{31}R_{13}-R_{41}R_{14}-R_{34}R_{43}-R_{32}R_{23}-R_{42}R_{24}$$

$$\begin{aligned}r_3=&R_{11}R_{32}R_{23}-R_{31}R_{12}R_{23}-R_{11}R_{22}R_{44}-R_{42}R_{23}R_{34}+R_{31}R_{22}R_{13}+R_{32}R_{23}R_{44}-R_{11}R_{22}R_{33}-R_{32}R_{43}R_{24}\\&-R_{21}R_{32}R_{13}+R_{11}R_{42}R_{24}+R_{31}R_{13}R_{44}+R_{21}R_{12}R_{44}-R_{21}R_{42}R_{14}+R_{42}R_{24}R_{33}+R_{21}R_{12}R_{33}-R_{11}R_{33}R_{44}\\&-R_{22}R_{33}R_{44}-R_{41}R_{12}R_{24}-R_{31}R_{43}R_{14}+R_{41}R_{22}R_{14}+R_{32}R_{34}R_{44}+R_{41}R_{14}R_{33}+R_{11}R_{34}R_{43}-R_{41}R_{13}R_{34}\end{aligned}$$

$$\begin{aligned}r_4=&-R_{41}R_{12}R_{23}R_{34}-R_{21}R_{12}R_{33}R_{44}+R_{11}R_{22}R_{33}R_{44}-R_{11}R_{42}R_{24}R_{33}+R_{21}R_{32}R_{13}R_{44}+R_{11}R_{32}R_{43}R_{24}\\&-R_{41}R_{32}R_{13}R_{24}+R_{41}R_{32}R_{23}R_{14}-R_{11}R_{22}R_{34}R_{43}+R_{21}R_{12}R_{34}R_{43}-R_{31}R_{12}R_{43}R_{24}-R_{21}R_{42}R_{13}R_{34}\\&-R_{21}R_{32}R_{43}R_{14}+R_{31}R_{12}R_{14}R_{44}+R_{31}R_{42}R_{13}R_{24}-R_{31}R_{42}R_{23}R_{14}+R_{21}R_{42}R_{14}R_{33}+R_{11}R_{42}R_{23}R_{34}\\&-R_{11}R_{32}R_{23}R_{44}+R_{31}R_{22}R_{43}R_{14}-R_{31}R_{22}R_{13}R_{44}+R_{41}R_{12}R_{24}R_{33}-R_{41}R_{22}R_{14}R_{33}+R_{41}R_{22}R_{13}R_{34}\end{aligned}$$

Use of Generative-AI tools declaration

The author declares he has not used Artificial Intelligence (AI) tools in the creation of this article.

Acknowledgments

The author extends his appreciation to Prince Sattam bin Abdulaziz University for funding this research work through the project number (PSAU/ 2025/01/34093).

Conflict of interest

The author declare that he has no known competing financial interests or personal relationships that could has appeared to influence the work reported in this paper.

References

1. A. A. Afaneh, R. A. Ibrahim, Nonlinear response of an initially buckled beam with 1:1 internal resonance to sinusoidal excitation, *Nonlinear Dynam.*, **4** (1993), 547–571. https://doi.org/10.1007/BF00162232
2. W. Yang, S. Towfighian, Internal resonance and low-frequency vibration energy harvesting, *Smart Mater. Struct.*, **26** (2017), 065034. https://doi.org/10.1088/1361-665X/aa791d
3. T. Inoue, Y. Ishida, Internal resonance phenomena of the Jeffcott rotor with nonlinear spring characteristics, *J. Vib. Acoust.*, **126** (2004), 476–484. https://doi.org/10.1115/1.1805000
4. K. L. Tuer, A. P. Duquette, M. F. Golnaraghi, Vibration control of a flexible beam using a rotational internal resonance controller. Part I: Theoretical development and analysis, *J. Sound Vib.*, **167** (1993), 41–62. https://doi.org/10.1006/jsvi.1993.1320
5. A. P. Duquette, K. L. Tuer, M. F. Golnaraghi, Vibration control of a flexible beam using a rotational internal resonance controller. Part II: Experiment, *J. Sound Vib.*, **167** (1993), 63–75. https://doi.org/10.1006/jsvi.1993.1321
6. A. H. Nayfeh, D. T. Mook, L. R. Marshall, Nonlinear coupling of pitch and roll modes in ship motions, *J. Hydronautics*, **7** (1973), 145–152. https://doi.org/10.2514/3.62949
7. K. R. Qalandar, B. S. Strachan, B. Gibson, M. Sharma, A. Ma, S. W. Shaw, et al., Frequency division using a micromechanical resonance cascade, *Appl. Phys. Lett.*, **105** (2014), 244–252. https://doi.org/10.1063/1.4904465
8. A. Z. Hajjaj, Z. Amal, M. A. Hafiz, M. I. Younis, Mode coupling and nonlinear resonances of MEMS arch resonators for band-pass filters, *Sci. Rep.*, **7** (2017), 41820. https://doi.org/10.1038/srep41820
9. A. Vyas, D. Peroulis, A. K. Bajaj, A micro-resonator design based on nonlinear 1:2 internal resonance in flexural structural modes, *J. Microelectromech. Syst.*, **18** (2009), 744–762. https://doi.org/10.1109/JMEMS.2009.2017081
10. M. Sayed, M. Kamel, 1:2 and 1:3 internal resonance active absorber for nonlinear vibrating systems, *Appl. Math. Model.*, **36** (2012), 310–332. https://doi.org/10.1016/j.apm.2011.05.057
11. X. Wei, R. Li, S. Li, Resonance and bifurcation in a nonlinear duffing system with cubic coupled terms, *Nonlinear Dynam.*, **46** (2006), 211–221. https://doi.org/10.1007/s11071-006-9024-1
12. L. Lipiäinen, A. Jaakkola, K. Kokkonen, M. Kaivola, Frequency splitting of the main mode in a microelectromechanical resonator due to coupling with an anchor resonance, *Appl. Phys. Lett.*, **100** (2012), 173720. https://doi.org/10.1063/1.3673558
13. C. V. D. Avoort, R. V. D. Hout, J. J. M. Bontemps, P. G. Steeneken, K. L. Phan, R. H. B. Fey, et al., Amplitude saturation of MEMS resonators explained by autoparametric resonance, *J. Micromech. Microeng.*, **20** (2010), 105012–105015. https://doi.org/10.1088/0960-1317/20/10/105012
14. R. S. Haxton, A. D. S. Barr, The autoparametric vibration absorber, *J. Sound Vib.*, **83** (1972), 440–443. https://doi.org/10.1016/S0022-460X(82)80115-6
15. L. Xiong, L. Tang, B. R. Mace, Internal resonance with commensurability induced by an auxiliary oscillator for broadband energy harvesting, *Appl. Phys. Lett.*, **108** (2016), 043901. https://doi.org/10.1063/1.4949557
16. A. H. Ramini, A. Z. Hajjaj, M. I. Younis, Tunable resonators for nonlinear modal interactions, *Sci. Rep.*, **6** (2016), 26674. https://doi.org/10.1038/srep34717

17. A. Z. Hajjaj, N. Jaber, M. A. A. Hafiz, S. Ilyas, M. I. Younis, Multiple internal resonances in MEMS arch resonators, *Phys. Lett. A*, **384** (2018), 3393–3398. https://doi.org/10.1016/j.physleta.2018.09.033
18. D. Antonio, D. H. Zanette, D. López, Frequency stabilization in nonlinear micromechanical oscillators, *Nat. Commun.*, **5** (2012), 806. https://doi.org/10.1038/ncomms1813
19. B. Jeong, C. Pettit, S. Dharmasena, H. Keum, J. Lee, J. Kim, et al. Utilizing intentional internal resonance to achieve multi-harmonic atomic force microscopy, *Nanotechnology*, **27** (2016), 245704. https://doi.org/10.1088/0957-4484/27/12/125501
20. R. Potekin, S. Dharmasena, H. Keum, X. Jiang, J. Lee, S. Kim, et al., Multi-frequency atomic force microscopy based on enhanced internal resonance of an inner-paddled cantilever, *Sens. Actuat. A-Phys*., **273** (2018), 206–220. https://doi.org/10.1016/j.sna.2018.01.063
21. H. K. Khalil, *Nonlinear systems*, 3 Eds., Prentice Hall: Upper Saddle River, NJ, USA, 2002.
22. X. Zhang, Y. Li, S. Wang, Nonlinear vibration control of flexible structures via integral resonance control with adaptive gains, *Mech. Syst. Signal Process.*, **168** (2022), 108563.
23. M. K. Hasan, H. Kim, J. H. Park, Robust positive position feedback control for vibration suppression of smart composite plates, *Smart Mater. Struct.*, **27** (2018), 115007.
24. J. L. Chen, P. Y. Chen, Nonlinear integral positive position feedback control of flexible beams with actuator saturation, *J. Sound Vib.*, **444** (2019), 11–25.
25. Y. Jiang, Y. Wang, Y. H. Wang, J. H. Yang, Y. J. Qian, Experimental and theoretical investigations of fiber-laying angle, graphene, and temperature effects on vibrational behaviors and nonlinear flutter in composite trapezoidal wing plates, *Eur. J. Mech. A-Solids*, **116** (2026), 105918. https://doi.org/10.1016/j.euromechsol.2025.105918
26. Y. Z. Lian, W. Zhang, B. Siriguleng, Snap-through and nonlinear vibrations of bistable ACPCL cantilever shells under combined external and parametric excitations: Theory and experiment, *Energy*, **336** (2025), 138513. https://doi.org/10.1016/j.energy.2025.138513
27. H. Yu, T. Hu, Q. Wang, Adaptive nonlinear PD controller with cubic velocity feedback for vibration suppression in high-speed flexible manipulators, *IEEE-ASME T. Mech.*, **26** (2021), 1324–1333.
28. S. Yang, Z. Liu, D. J. Inman, Nonlinear damping control for vibration reduction in flexible structures: A survey and recent advances, *Nonlinear Dynam.*, **98** (2019), 1785–1805.
29. W. Zuo, Y. Wang, H. Gao, Comparison of nonlinear control schemes for vibration suppression of multi-degree-of-freedom systems, *J. Vib. Control*, **29** (2023), 2045–2060.
30. C. H. He, Y. Cui, J. H. He, E. Buhe, Q. Bai, Q. Xu, et al., Nonlinear dynamics in MEMS systems: Overcoming pull-in challenges and exploring innovative solutions, *J. Low Freq. Noise V. A.*, 2025, 1−33.
31. C. Xia, D. F. Wang, T. Ono, T. Itoh, R. Maeda, A mass multi-warning scheme based on one-to-three internal resonance, *Mech. Syst. Signal Process.*, **142** (2020), 106784. https://doi.org/10.1016/j.ymssp.2020.106784
32. A. H. Nayfeh, *Introduction to perturbation techniques*, Wiley: New York, NY, USA, 1993.
33. A. H. Nayfeh, *Perturbation methods*, Wiley: New York, NY, USA, 1973.
34. A. H. Nayfeh, D. T. Mook, *Nonlinear oscillations*, Wiley: New York, NY, USA, 1979.
35. R. Starosta, G. S. Kamińska, J. Awrejcewicz, Asymptotic analysis of kinematically excited dynamical systems near resonances, *Nonlinear Dynam.*, **68** (2012), 459–469. https://doi.org/10.1007/s11071-011-0229-6

36. S. Rajasekar, M. A. F. Sanjuán, Nonlinear resonances, Springer: Cham, Switzerland, 2016. https://doi.org/10.1007/978-3-319-24886-8
37. X. He, A. Mohammadian, Frequency correction for nonlinear coupled multi-DOF systems with cubic stiffness, *Front. Mech. Eng.*, **25** (2025), 028.

AIMS Press